The Astrophysical Journal, 965:105 (19pp), 2024 April 20 https://doi.org/10.3847/1538-4357/ad2940

Multiphase Gas in Elliptical Galaxies: The Role of Type Ia Supernovae

Rajsekhar Mohapatra and Eliot Quataert
Department of Astrophysical Sciences, Princeton University, Princeton, NJ 08544, USA; rmohapatra@princeton.edu
Received 2023 December 15; revised 2024 February 1; accepted 2024 February 12; published 2024 April 11

Abstract

Massive elliptical galaxies harbor large amounts of hot gas ($T \gtrsim 10^6$ K) in their interstellar medium (ISM) but are typically quiescent in star formation. The jets of active galactic nuclei (AGNs) and Type Ia supernovae (SNe Ia) inject energy into the ISM, which offsets its radiative losses and keeps it hot. SNe Ia deposit their energy locally within the galaxy compared to the larger few $\times 10$ kiloparsec-scale AGN jets. In this study, we perform high-resolution (512^3) hydrodynamic simulations of a local (1 kpc^3) density-stratified patch of the ISM of massive galaxies. We include radiative cooling and shell-averaged volume heating, as well as randomly exploding SN Ia. We study the effect of different fractions of supernova (SN) heating (with respect to the net cooling rate), different initial ISM density/entropy (which controls the growth time $t_{\rm ti}$ of the thermal instability), and different degrees of stratification (which affect the freefall time $t_{\rm ff}$). We find that SNe Ia drive predominantly compressive turbulence in the ISM with a velocity dispersion of σ_v up to 40 km s^{-1} and logarithmic density dispersion of $\sigma_s \sim 0.2$–0.4. These fluctuations trigger multiphase condensation in regions of the ISM, where $\min(t_{\rm ti})/t_{\rm ff} \lesssim 0.6\exp(6\sigma_s)$, in agreement with theoretical expectations that large density fluctuations efficiently trigger multiphase gas formation. Since the SN Ia rate is not self-adjusting, when the net cooling drops below the net heating rate, SNe Ia drive a hot wind which sweeps out most of the mass in our local model. Global simulations are required to assess the ultimate fate of this gas.

Unified Astronomy Thesaurus concepts: Early-type galaxies (429); Interstellar medium (847); Type Ia supernovae (1728); Cooling flows (2028)

1. Introduction

The interstellar medium (ISM) in massive galaxies is hot, with temperatures $T \sim 10^6$–10^7 K, and the dense central regions (number density $n \sim 0.01$–1 cm^{-3}) can cool in less than 1 Gyr (Werner et al. 2012). However, the ISM in most of these early-type galaxies is not undergoing a cooling flow (Peterson et al. 2003). They show little to no current star formation, and their stellar populations are typically $\gtrsim$10 Gyr old, barring a few exceptions (see, e.g., Calzadilla et al. 2022). Hence, the ISM of these massive ellipticals needs to be heated constantly to keep them in a roughly thermal balance, see Donahue & Voit (2022) for a recent review.

Heating of the ISM due to the jets of active galactic nuclei (AGNs) powered by the accretion of matter onto the supermassive black hole is one significant energy source (e.g., Allen et al. 2006; Fabian 2012; Gaspari et al. 2017; Main et al. 2017; Guo et al. 2023). AGN jets are typically found to deposit their energy further out (few $\times 10$ kpc) from the central regions of the galaxy (Bîrzanet al. 2004). However, on approximately kiloparsec scales, the jets are highly collimated and the cavities/bubbles associated with them are not volume filling. While the mechanical energy input from AGN jets matches the net cooling of the halo gas in several systems (McNamara & Nulsen 2007; Rafferty et al. 2008; Olivares et al. 2023), the distribution of this heating throughout the ISM is still an open question.

Heating due to supernovae (SNe) is another attractive model. In early-type galaxies with old stellar populations, Type Ia supernovae (SNe Ia) dominate the stellar energy output channel and are a natural outcome of stellar evolution. The spatial distribution of SNe Ia is expected to follow the stellar distribution in the galaxy. Hence, these SNe deposit their energy more uniformly and within the ISM of the galaxy compared to the AGN jets. Studies such as that of Voit et al. (2015) have shown that the energy injected by SNe Ia exceeds the energy lost due to radiative cooling in the high-entropy outer regions of elliptical galaxies. They propose that the mass deposited into the ISM by asymptotic giant branch (AGB) stars can be swept out by an SN Ia-driven wind, helping to keep the ISM density low and its cooling time ($t_{\rm cool}$) long. Li et al. (2018) find that supernova (SN) heating can suppress star formation in low-mass ellipticals, while AGN feedback is more efficient for systems with stellar mass $\gtrsim 10^{11} M_\odot$ (also see Ciotti 1991; Conroy et al. 2015; Voit et al. 2020; Molero et al. 2023).

Since the net energy output of SNe Ia is lower than that of the AGN outbursts, many individual galaxy/galaxy cluster-scale simulations have ignored their effect. Cosmological simulations have generally included the mass and the injection of energy, due to the SNe using sub-grid models (e.g., Crain et al. 2015; Pillepich et al. 2018). Alternatively, in simulations that do include discrete SNe (e.g., Su et al. 2019) it is not clear whether they have the resolution to resolve individual supernova remnants (SNRs) of a size of a few $\times 10$ pc in the low-density ISM of massive ellipticals. While the injection of energy due to SNe is accounted for by such models, they cannot account for the small-scale turbulence driven by the remnants (on scales of 50–100 pc) and the density fluctuations they generate. These density fluctuations can trigger multiphase condensation in the halo gas if the ratio of the growth time of the thermal instability to the freefall time ($t_{\rm ti}/t_{\rm ff}$, Sharma et al. 2012; Choudhury et al. 2019) or the ratio of $t_{\rm ti}$ to the mixing time ($t_{\rm ti}/t_{\rm mix}$, Gaspari et al. 2018; Mohapatra & Sharma 2019) falls below a critical density dispersion amplitude (σ_s)-dependent ratio (Voit 2021;

Mohapatra et al. (2023, hereafter M23). Observational studies such as that of Olivares et al. (2019) report multiphase filamentary structures around the brightest cluster galaxies in low-entropy and short cooling time regions of clusters.

Numerical studies on small scales ($\lesssim$10 kpc regions) can resolve individual remnants, either by implementing mesh-refinement techniques around the SN injection regions or modeling even smaller, less than or equivalent to kiloparsec-scale regions of the ISM with uniform resolution. For example, Tang et al. (2009a, 2009b) looked at the role played by SNe Ia in the Milky Way's bulge. They find that SNe Ia power a galactic bulge wind with a filamentary structure. This wind sweeps out mass from the inner regions and keeps the circumgalactic medium (CGM) hot.

In the context of massive elliptical galaxies, Li et al. (2020a, 2020b, hereafter MLi20a and MLi20b, respectively) modeled small patches (of a size of approximately a few $\times$100 pc) of the ISM at different distances from the galactic center. They show that the nonuniform heating by SNe produces multiphase gas even when the net heating rate moderately exceeds the net cooling rate. They also report that the heating by SNe Ia is different from uniformly injected volume heating—the localized heating caused by SNe Ia drives compressive turbulence and produces large density fluctuations in the ISM. However, MLi20a and MLi20b did not include an external gravitational field in their setup. In a stably stratified atmosphere, buoyancy effects can suppress the formation of cold gas if $t_{\rm ti}/t_{\rm ff}$ is large enough. The SN-heated bubbles would rise against gravity and generate convective instabilities (such as the Rayleigh–Taylor instability), which can generate solenoidal turbulence and increase the mixing rate of the SNe ejecta with the ambient ISM. Further, an overheated atmosphere would drive an outflowing wind (as reported by Tang et al. 2009b, in the context of the Milky Way's bulge). Such a wind can transfer energy, mass, and metals to outer regions of the galaxy. Thus, an external gravitational field is expected to play a critical role in understanding the impact of SNe Ia on the ISM of massive galaxies.

A parallel set of calculations has been used to study the onset of thermal instability in stratified plasmas and the impact of ambient turbulence (and/or seed perturbations) on this process (e.g., Parrish et al. 2010; Choudhury & Sharma 2016; Voit 2018; Choudhury et al. 2019; M23). This is important for understanding the origin of multiphase gas in massive galaxies, groups, and clusters, and its role in fueling star formation and black hole growth. Such calculations typically either seed the initial density fluctuations of a fixed amplitude or drive turbulence on large scales. MLi20b have shown that the properties of turbulence driven by small-scale SN Ia remnants are quite different from the large-scale forcing typically employed in turbulence simulations. The remnants typically drive turbulence on sub-100 pc scales with a large compressive to solenoidal ratio and seed much larger density perturbations than expected from σ_s–$\mathcal{M}$ (rms Mach number) scaling relations in forced turbulence (Federrath et al. 2008, 2010; Konstandin et al. 2012). These differences in driving can affect the mixing rate between the hot remnants and the ambient ISM, as well as the occurrence of multiphase condensation for a given set of turbulence parameters.

In this work, we aim to study the properties of the energy injected by SN Ia in a density-stratified, kiloparsec-scale patch model of the ISM. We conduct hydrodynamic simulations including randomly injected SNe, radiative cooling, and shell-by-shell volume heating. In our fiducial set, we study the effect of increasing SN injection rate on multiphase condensation, properties of turbulence in the ISM, and the development of an SN Ia-powered wind. We also check the dependence of our results on the ambient stratification (which control $t_{\rm ff}$), different initial gas densities (which affect $t_{\rm ti}$) as well as the effect of including mass ejected from AGB stars. We note from the outset that our study is restricted to local simulations that model a patch of the ISM/intracluster medium (ICM). These calculations are analogous to the extensive literature on simulations of the impact of core-collapse SNe on the ISM of disk galaxies (e.g., Kim & Ostriker 2015; Martizzi et al. 2015; Fielding et al. 2017). One important difference is that the local approximation is much less motivated for the Type I/elliptical galaxy application because of the absence of a thin disk. However, given the extensive literature on local simulations in studying the onset of thermal instability, it is valuable to assess the role of SNe Ia in that context before proceeding to global simulations.

In the next section, we introduce some of the theoretical background and estimate the different relevant energy sources and sinks. We state our model and numerical methods in Section 3. In Section 4, we present the results from our fiducial set of simulations, where we progressively increase the SN Ia heating rate keeping all other parameters constant. We study the effect of other simulation parameters and summarize the astrophysical implications of this work in Section 5. We discuss our caveats and prospects in Section 6, and finally, conclude in Section 7.

2. Theoretical Background

2.1. Analytic Estimates

In this section, we begin by providing some estimates of the different energy sources and sinks for the typical massive elliptical galaxies studied in Werner et al. (2012, 2014).

2.1.1. Radial Profiles of Stars, Gas Density, and Entropy

We first obtain the radial profiles of gas number density n and entropy S from Figure 6 of Werner et al. (2012). We normalize the gas number density $n = 0.07\ {\rm cm}^{-3}$ and entropy $S_0 = 6.8\ {\rm keV\ cm}^2$ at $r = 2$ kpc, in agreement with the X-ray observations. The entropy profile flattens in the center and follows a power-law scaling $\propto r^1$ at large r. In the upper panel of Figure 1, we show the radial profiles of gas number density n, stellar mass density ρ_*, and entropy S.

For calculating the stellar mass distribution, we assume a Hernquist profile (Hernquist 1990) with $m_* = 2 \times 10^{11} M_\odot$ (see Table 1 in Merritt & Ferrarese 2001, for typical bulge masses of these galaxies) and $r_* = 2$ kpc ($r_* \approx r_{\rm eff}/1.8$, we obtain $r_{\rm eff}$ using the mass–size relations from Figure 1 of Trujillo et al. 2011).

2.1.2. Cooling Rate of the Hot ISM

The ISM of an early-type galaxy is generally hot, with temperatures of around 10^6–10^7 K. It cools through free–free Bremsstrahlung emission and far-UV/X-ray line emission. In order to calculate the cooling rate, we set the gas metallicity to $Z = 0.5 Z_\odot$ and generate a temperature-dependent cooling table $\Lambda(T)$ using Grackle (Smith et al. 2017). The cooling rate

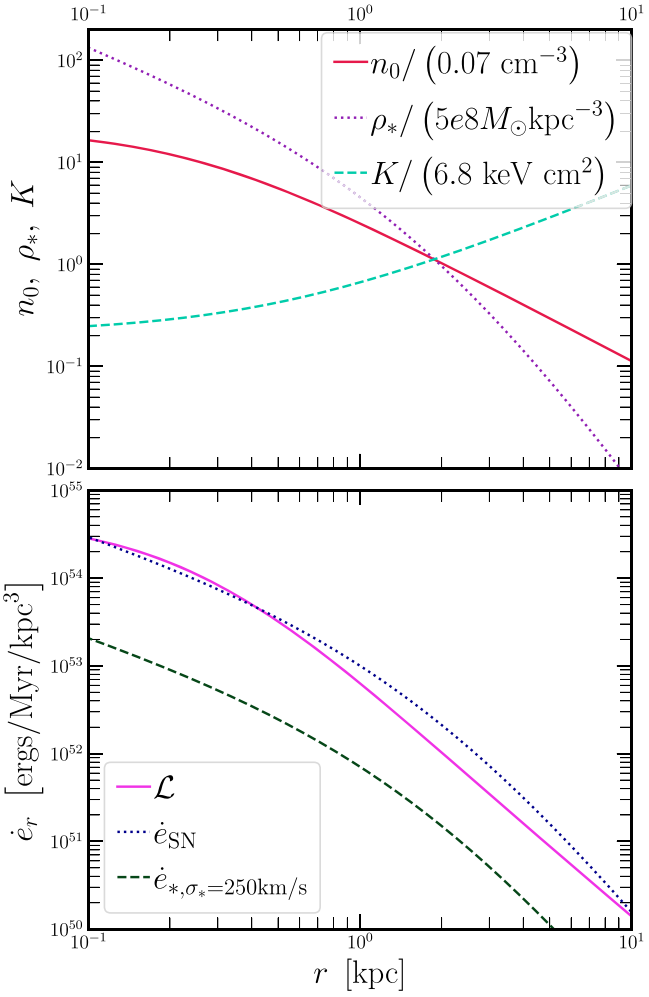

Figure 1. Upper panel: radial profiles of gas number density n, stellar mass density ρ_*, and entropy S for a typical massive elliptical galaxy, normalized to their values at 2 kpc. Lower panel: radial profiles of the cooling rate density $\mathcal{L}$, SN heating rate density $\dot{e}_{\rm SN}$, and stellar wind heat rate density $\dot{e}_*$, assuming the stellar velocity dispersion of $\sigma_* = 250$ km s^{-1}.

density $\mathcal{L}$ is given by

$$\mathcal{L} = n^2 \Lambda(T). \tag{1a}$$

We show $\mathcal{L}$ as a function of r in the lower panel of Figure 1.

2.1.3. Heating due to SN Ia

For a stellar population of age $\sim$10 Gyr, the SN Ia energy injection rate is given by

$$\dot{E}_{\rm SN} \simeq 10^{51}\,\mathrm{erg} \times 300(\mathrm{Myr})^{-1}(M_*/10^{10}\,M_\odot), \tag{1b}$$

assuming that each SN injects $E_{\rm SN} = 10^{51}$ erg of energy and that the SN Ia goes off at a rate $300(\mathrm{Myr})^{-1}(M_*/10^{10}\,M_\odot)$, consistent with the delay-time distribution of the SN Ia in Maoz & Graur (2017; see also Scannapieco & Bildsten 2005; Barkhudaryan 2019). We show $\dot{e}_{\rm SN}$ ($\dot{E}_{\rm SN}$ per unit volume) in the lower panel of Figure 1. While the exact values of the cooling rate and the SN heating rate will vary across different systems, the comparison in Figure 1 indicates that the SN heating rate is likely within an order of magnitude of the cooling rate density within the central 10 kpc of the ISM in massive galaxies. This emphasizes the potential importance of SNe Ia as a heating source that can compensate for cooling losses and affect the development of thermal instability. *This is one of the main motivations for studying the effect of SN Ia heating in local patches of the ISM.*

2.1.4. Heating due to Thermalization of Stellar Winds

Stars on the AGB eject their outer envelopes into the ISM, at a rate of

$$\dot{M}_* = M_* \times 2.5 \times 10^{-6}\,\mathrm{Myr}^{-1}, \tag{1c}$$

assuming a stellar age of $\sim$10 Gyr and using the models in Conroy et al. (2009). Since the stars typically have a velocity dispersion of $\sigma_* \sim 200$–300 km s^{-1} with respect to the ISM, the wind material can become thermalized with the ISM and contribute to its heating.[1] The heating rate density due to the stellar winds is given by

$$\dot{e}_* = \dot{M}_* \sigma_*^2 = 2.5 \times 10^{-6} M_* \sigma_*^2 \mathrm{Myr}^{-1}. \tag{1d}$$

We show the radial profile of $\dot{e}_*$ in the lower panel of Figure 1, assuming $\sigma_* = 250$ km s^{-1}. The stellar heating rate density is roughly an order of magnitude smaller than the cooling rate density and the SN heating rate density. However, it could be more important in compact galaxies with large σ_*, as discussed in Conroy et al. (2015).

2.2. Condition for the Absence of Shell Formation

In the standard picture of an SN going off in the ISM (see Chapter 39 in Draine 2011), the evolution of the remnant can be divided into four stages—(1) free-expansion, (2) Sedov–Taylor phase (energy conservation), (3) snowplow phase (where a dense cooling shell forms from the swept-up material) and (4) fadeaway (where the shock wave fades into a sound wave in pressure equilibrium with the ambient medium). In the early-type galaxies considered in this study, the ISM is hotter (temperature $T \gtrsim 10^6$ K) and has a lower density ($n \lesssim 0.1\,\mathrm{cm}^{-3}$) compared to typical conditions in a galactic disk. Under such conditions, the shock wave may reach pressure equilibrium before the snowplow phase, i.e., before the onset of significant cooling losses (MLi20a).

The fade radius $R_{\rm fade}$, at which the shock wave evolves into a sound wave is given by

$$\begin{aligned} R_{\rm fade} &= \left(\alpha(\gamma-1)\frac{E_{\rm SN}}{4\pi P/3}\right)^{1/3} \\ &= 46.0\ \mathrm{pc}\ \alpha^{1/3}(E_{\rm SN}/10^{51}\,\mathrm{erg})^{1/3} \\ &\quad \times (n/0.08\ \mathrm{cm}^{-3})^{-1/3}(T/3\times10^6\ \mathrm{K})^{-1/3}, \end{aligned} \tag{2a}$$

where P and T are the pressure and temperature of the ambient ISM, respectively, and α is a free parameter of order unity. The fade radius is less than the radius at end of the Sedov–Taylor phase (when strong cooling commences) when the ambient density n falls below a critical number density $n_{\rm crit}$, which is

[1] The AGB ejecta may not always become fully mixed with the ISM and may survive as cold gas embedded in the hot ISM, especially in high-pressure environments; see Li et al. (2019) for a detailed study. For simplicity, we have ignored this effect in our calculations.

given by MLi20a as

$$n_{\rm crit} = 7.56\ {\rm cm}^{-3}(T/(3\times10^6\ {\rm K})/\alpha)^{3.85}\sqrt{E_{\rm SN}/10^{51}\ {\rm erg}}. \quad (2b)$$

The strongest dependence in Equation (2b) is on the temperature of the ambient medium. Higher temperatures—when the temperature is above the peak of the atomic cooling curve—correspond to less efficient cooling and higher ambient pressure, both of which lead to the SNR reaching pressure equilibrium prior to significant cooling losses. The condition $n < n_{\rm crit}$ is satisfied for most regions of the ISM in the early-type galaxies that we study.

3. Methods

3.1. Model Equations

We use Euler equations to model the ISM as an ideal gas with an adiabatic index of $\gamma = 5/3$. We evolve the following equations:

$$\frac{\partial\rho}{\partial t} + \nabla\cdot(\rho\boldsymbol{v}) = \dot{n}_{\rm SN}M_{\rm SN} + \dot{\rho}_*, \quad (3a)$$

$$\frac{\partial(\rho\boldsymbol{v})}{\partial t} + \nabla\cdot(\rho\boldsymbol{v}\otimes\boldsymbol{v}) + \nabla P = \rho\boldsymbol{g}, \quad (3b)$$

$$\frac{\partial e}{\partial t} + \nabla\cdot((e+P)\boldsymbol{v}) = -\rho(\boldsymbol{v}\cdot\nabla)\Phi + \dot{e}_{\rm SN} + \dot{e}_* + \dot{e}_{\rm shell} - \mathcal{L}, \quad (3c)$$

$$e = \frac{\rho\boldsymbol{v}\cdot\boldsymbol{v}}{2} + \frac{P}{\gamma-1}, \quad (3d)$$

where ρ is the gas mass density, $\boldsymbol{v}$ is the velocity and $P = \rho k_{\rm B}T/(\mu m_p)$, where $\mu \approx 0.6m_p$ is the mean particle weight, m_p is the proton mass, and $k_{\rm B}$ is the Boltzmann constant. In the continuity equation (Equation (3a)), $n_{\rm SN}$ denotes the rate of SN injection per unit volume and $M_{\rm SN}$ denotes the mass injected by each SN. In addition to the mass injected by SNe, we also include the contribution of AGB winds, denoted by $\dot{\rho}_*$ (only in a subset of our simulations). We denote the acceleration due to gravity as $\boldsymbol{g}$ in the momentum Equation (3b). In the energy equation (Equation (3c)), the total energy density is given by E and the gravitational potential is denoted by Φ, with $\boldsymbol{g} = -\nabla\Phi$. We include $\mathcal{L}$, $\dot{e}_{\rm SN}$ and $\dot{e}_*$ defined by Equations (1a)–(1d), as well as a shell-by-shell heating rate density $\dot{e}_{\rm shell}$.

3.2. Numerical Methods

We perform hydrodynamic simulations using a performance portable version of the Athena++ (Stone et al. 2020) code implemented using the Kokkos library (Trott et al. 2021). We use the second-order Runge–Kutta time integrator, the Harten–Lax–van Leer contact Riemann solver, and the piece-wise linear spatial reconstruction method. For cells with unphysically large velocities or temperatures, we use a first-order flux correction algorithm described in the appendix in Lemaster & Stone (2009).

3.2.1. Domain Size and Decomposition

We simulate a cuboidal patch of the ISM with dimensions $L\times L\times 1.5\,L$ using a Cartesian grid, where $L = 1$ kpc and the longer dimension is oriented along the z-direction. By default, we divide the simulation domain into a grid size of $512\times512\times768$, such that each resolution element is cubical in size (i.e., $dx = dy = dz$). Our simulation box is centered at the origin (0, 0, 0).

3.2.2. Boundary Conditions

Similar to M23, we use periodic boundary conditions along the x- and y-directions. The proper boundary conditions in the vertical direction for this problem are nontrivial in that if an SN-driven outflow develops, one would like boundary conditions that allow such an outflow (and allow the density and pressure at the boundary to change). If an outflow does not develop, the boundary conditions should maintain hydrostatic equilibrium with densities and pressures similar to the initial condition. After experimentation, we settled on a compromise in which we use constant boundary conditions for ρ and P at the z-boundaries. At the upper z-boundary, we implement diode boundary conditions for the z-direction velocity v_z. At the lower boundary, we set $v_z = 0$ for gas with $T \gtrsim T_{\rm floor}$ and diode otherwise. Setting $v_z = 0$ at the lower boundary prevents the atmosphere from undergoing a global collapse and the second condition prevents cold-infalling gas from gathering in the negative z-direction.

To minimize the impact of the boundary conditions on our results, we treat the regions beyond $|z| > 0.5\,L$ as boundary regions and do not include them while analyzing the results of our simulations.

3.3. Problem Setup

3.3.1. Initial Density and Pressure Profiles

We set up a gravitationally stratified atmosphere with a constant $\boldsymbol{g}$ oriented along the $-\hat{\boldsymbol{z}}$ direction. At time $t = 0$, pressure and density follow exponentially decreasing profiles along the $+\hat{\boldsymbol{z}}$ direction and the gas is at hydrostatic equilibrium. The initial z-profiles are given by

$$P(t=0) = P_0\exp\left(-\frac{z}{H}\right), \quad (4a)$$

$$\rho(t=0) = \frac{P(t=0)}{gH}, \quad (4b)$$

where H is the scale height of the pressure/density and P_0, ρ_0 ($=P_0/gH$) are the initial values of pressure and density at $z = 0$, respectively.

3.3.2. SN Injection

The SN heating rate density $\dot{e}_{\rm SN}$ is given by

$$\dot{e}_{\rm SN} = \dot{n}_{\rm SN}E_{\rm SN}. \quad (5a)$$

In our local ISM patch simulations, we set

$$\dot{n}_{\rm SN} = \dot{n}_0\exp(-z/H_{\rm SN}), \quad (5b)$$

such that the net heating rate due to SN is

$$\dot{N}_{\rm SN}E_{\rm SN} = f_{\rm SN}\int\mathcal{L}_0dV, \text{ where} \quad (5c)$$

$$\dot{N}_{\rm SN} = \int\dot{n}_{\rm SN}dV, \quad (5d)$$

and $f_{\rm SN}$ is a parameter that sets the normalization of the SN heating rate. In the above set of equations, $H_{\rm SN}$ denotes the

scale height of the stellar/SN distribution, $\mathcal{L}_0$ is the cooling rate at $t = 0$ and $f_{\rm SN}$ is a parameter that we vary across simulations. We set $H_{\rm SN} = 0.5H$ so that the heating rate by an SN has the same variation with z as $\mathcal{L}$ ($\mathcal{L} \propto \rho^2 \propto \exp(-z/0.5H)$), motivated in part by the observations shown in Figure 1. As we shall show, even with an initial condition balancing heating and cooling both globally and as a function of z, the simulations with significant SN Ia heating tend to rapidly blow a significant amount of gas out of the box. We tried other values of $H_{\rm SN}/H$ as well, and found that in those cases, the transition to rapid blowout happened even more quickly.

We fix $f_{\rm SN}$ at $t = 0$, which sets $\dot{N}_{\rm SN}$. The expected number of SNe in a time step dt is given by $\dot{N}_{\rm SN} dt$. We draw the total number of SNe in a given time step from a Poisson distribution with this mean. We obtain the x and y coordinates of the center of the remnant from a uniform distribution and use an exponential distribution for the z coordinate.

The SN Ia remnants in the ISM of an elliptical galaxy are not expected to undergo a snowplow phase (see Section 2.2) and remain in the energy-conserving phase until they fade away into sound waves. Once the center of an individual remnant is determined, we inject $E_{\rm SN} = 10^{51}$ erg of energy as thermal energy and $M_{\rm SN} = M_\odot$ of mass inside a sphere of radius $0.6 \times R_{\rm fade}$. Since our simulations have a spatial resolution of $\sim$2 pc, each remnant is resolved by $\gtrsim$10 cells.

3.3.3. Heating due to AGB Winds

In a few of our simulations, we have included the effect of mass and energy added to the ISM due to ejecta from AGB stars. We assume that the AGB wind material is thermalized with the ambient ISM. After setting $\dot{N}_{\rm SN}$ using Equation (5c), we obtain $\dot{M}_*$ and $\dot{e}_*$ using Equations (1b)–(1d) and $\sigma_* = 250\,{\rm km\,s^{-1}}$. We inject mass and energy into the ISM with the same z-dependence as the SN injection ($\propto \exp(-z/H_{\rm SN})$). Although we do not include the effect of AGB winds in our fiducial set, we discuss their impact in the Appendix.

3.3.4. Modifications to the Cooling Function

To control the code time step set by the cooling function, we reduce $\mathcal{L}$ to zero for $T < T_{\rm cutoff}$. The modified cooling function is given by

$$\mathcal{L} = n^2 \Lambda(T) \exp(-10(T_{\rm floor}/T)^4), \tag{5e}$$

where we set $T_{\rm floor} = 3 \times 10^4$ K.

3.3.5. Thermal Heating Rate and Shell-by-shell Energy Balance

To study the impact of different fractions of SN heating with respect to the net cooling, as well as to prevent a runaway cooling flow, we implement an additional heating source $\dot{e}_{\rm shell}$, which replenishes a $(1 - f_{\rm SN})$ fraction of the energy lost due to cooling of hot gas ($T \geqslant T_{\rm hot} = 10^{5.5}$ K) in every z-shell at each time step. This method is a useful toy model that is agnostic to the origin of other sources of heating (such as AGN, radiation, cosmic rays, conduction, etc.) and has been used in many previous studies, such as those of Sharma et al. (2012), Choudhury et al. (2019), and M23. Despite its simple prescription, it leads to results similar to those of feedback heating (Gaspari et al. 2012; Prasad et al. 2015). Mathematically, this is given by

$$\dot{e}_{\rm shell} = \frac{\rho(x, y, z, t) \int \mathcal{L}(1 - f_{\rm SN}) \exp(-10(T_{\rm hot}/T)^4) dx dy}{\int \rho dx dy}. \tag{5f}$$

3.3.6. Important Timescales

The different relevant timescales of our setup are the Brunt–Väisälä oscillation time,

$$t_{\rm BV} = \sqrt{\gamma H_S/g}, \quad \text{where } H_S = (\gamma - 1)H, \tag{6a}$$

the turbulent mixing time,

$$t_{\rm mix} = \ell_{\rm int,sol}/v_{\rm int,sol} \text{ where,} \tag{6b}$$

$$\ell_{\rm int,sol} = 2\pi \frac{\int k^{-1} E_{\rm sol}(k) dk}{\int E(k)_{\rm sol} {\rm d}k},$$

the gravitational freefall time,

$$t_{\rm ff} = \sqrt{2H/g}, \tag{6c}$$

the cooling time,

$$t_{\rm cool} = \frac{n k_{\rm B} T}{(\gamma - 1) n^2 \Lambda(T)}, \tag{6d}$$

and the thermal instability growth time,

$$t_{\rm ti} = \frac{\gamma t_{\rm cool}}{2 - d\ln\Lambda/d\ln T - \alpha_{\rm heat}} \approx \gamma t_{\rm cool} \text{ at } T = T_0, \tag{6e}$$

$$\text{using } (d\ln\Lambda/d\ln T)_{T=T_0} \approx 0 \text{ and } \alpha_{\rm heat} = 1. \tag{6f}$$

In the above set of equations H_S is the scale height of entropy, k is the wavenumber, $E_{\rm sol}(k)$ is the power spectrum of the divergence-free (or solenoidal) component of the velocity field, $v_{\rm int,sol}$ is the solenoidal component of velocity on the integral scale $\ell_{\rm int,sol}$, $\alpha_{\rm heat}$ is defined such that $\dot{e}_{\rm shell} \propto \rho_{\rm heat}^{\alpha}$, and $n_{\rm bub}$ and $v_{\rm bub}$ are the number density and the velocity of the bubble inflated by an SNR, respectively.

3.4. Initial Conditions

We conduct a variety of simulations to model small patches of the ISM of an elliptical galaxy at different locations away from the galactic center. For all our simulations, we initialize the gas at a constant initial temperature $T_0 = 3 \times 10^6$ K, which is consistent with typical ISM temperatures in elliptical galaxies (see, e.g., Figure 1 in Voit et al. 2015). For our fiducial set of simulations, we set $n_0 = 0.08\,{\rm cm^{-3}}$ (at roughly 2 kpc out in Figure 1), motivated by observations of gas a few kiloparsecs from the center of massive galaxies, see, e.g., Figure 1 in Voit et al. (2015). At $t = 0$, we seed density fluctuations $\delta\rho/\rho$ in the gas, with 20% amplitude and a flat power spectrum (i.e., no scale dependence). These are consistent with measurements of X-ray brightness fluctuations (see, e.g., Zhuravleva et al. 2018, albeit on somewhat larger scales compared to our setup). Previous studies such as those of Choudhury et al. (2019), Voit (2021), and M23 have shown that a stratified, thermally unstable medium is expected to become multiphase if the ratio $t_{\rm ti}/t_{\rm ff}$ becomes smaller than a $\delta\rho/\rho$-dependent threshold. We choose the density/pressure

scale height of $H = 12$ kpc such that the initial t_{ti}/t_{ff} is close to the condensation threshold proposed by M23. Since we expect the SN driving to generate further density fluctuations in the ISM (as seen in MLi20b), our choice of initial conditions lets us directly study their impact on multiphase condensation. Our choice of H and T are also consistent with the observed profiles of density and temperature (at a few kiloparsecs from the center) in massive galaxies that host extended multiphase filaments (see blue scatter points in Figure 1 of Voit et al. 2015, for reference).

3.5. List of Simulations

For this study, we conducted a total of 16 simulations, which are listed in Table 1. We mainly study the effect of varying the fraction of the SN heating rate with respect to the net cooling rate. For our fiducial set, we conduct four simulations with $f_{SN} = 0.01$, 0.1, 0.5, and 0.99, as indicated in their respective simulation labels. In addition to understanding the effects of resolved SN Ia heating, our parameter choices are motivated by the inferred ratio between the heating and cooling rates observations of massive elliptical galaxies (Werner et al. 2012, 2014; Voit et al. 2015). For example, we find that in massive ellipticals, such as NGC 5846 and NGC 5044, which have a flat gas entropy profile, beyond the inner 10 kpc the stellar density (and as a result the SN Ia heating rate) drops off much faster with increasing radius compared to the net cooling rate. So heating due to SN Ia could dominate in the core, but other heating sources are expected to contribute in the outskirts.

To check the effect of a faster cooling rate, we repeat the fiducial set with double the initial density ($n_0 = 0.16\,\mathrm{cm}^{-3}$) and smaller initial seed density fluctuations ($\delta\rho/\rho = 0.05$). These runs are indicated by hdens in the simulation label.

For all of our other parameter choices, we conduct a pair of simulations—one with a small SN heating fraction ($f_{SN} = 0.01$) and another with a large SN heating fraction ($f_{SN} = 0.99$). The observed galaxies have different densities, temperatures, and strengths of stratification, which also vary across the inner and outer regions of the ISM. The ldens runs are useful to study the effect of a weaker cooling rate due to their smaller initial gas density. We conduct a pair of simulations with smaller density/pressure scale heights—*H*6hdens to look for the effect of stronger stratification on the hdens runs. Our *H*3 runs have initial density profiles that are directly comparable to that of a massive elliptical galaxy (see Figure 1), noting that we use a slightly cooler T_0. Finally, the $\dot{m}$ runs include mass and energy injection due to mass loss from AGB stars, as described in Section 3.3.3 (all other runs do not account for AGB winds).

We evolve all the simulations until $t_{end} = 500$ Myr. We define t_{mp} as the time at which the fraction of gas mass at $T < 10^{4.2}$ K exceeds 1% for the first time. For all simulations that have more than 1% of their total mass in the cold phase, we list t_{mp} in column (5) of Table 1, otherwise we denote $t_{mp} > 500$ Myr. In columns (6)–(12) we present different statistical properties of the simulations, averaged over the last 15 Myr of their evolution before t_{mp} (or t_{end} if they never have $M_{cold}/M_{tot} > 0.01$ during the simulation). For simulations where $t_{mp} \leqslant 30$ Myr, we present the statistical properties for $15\,\mathrm{Myr} \leqslant t < t_{mp}$, to allow enough time for the system to evolve before we analyze them.

We rerun all 16 simulations listed in Table 1 at half the resolution (using $256^2 \times 384$ resolution elements) and find all of the simulation properties listed in columns (5)–(12) to be within a few percent of their high-resolution counterparts.

4. Results of the Fiducial Runs

We start by presenting results from our fiducial runs, where we progressively increase the fraction of the SN Ia heating rate with respect to the net cooling rate. We study the effect of this parameter (f_{SN}) on the distributions of thermodynamic quantities such as density and temperature, time evolution of mass and energy, formation of cold gas ($T \lesssim 10^{4.2}$ K), and vertical shell-averaged profiles of energy fluxes. As we shall see, an important feature of our results is that when SN Ia heating is important (larger f_{SN}), there is no local equilibrium between SN heating and cooling possible. SNe eventually drive gas out of the box, decreasing the cooling rate, leading to stronger SN-driven wind, etc. The longer timescale outcome of this inevitable instability cannot be studied in our local approximation and will ultimately require global simulations.

4.1. Projection Maps

In Figure 2, we show snapshots of the x-projections of the logarithms of gas number density $\log_{10}(n_x)$ (column (1)), mass-weighted temperature $\log_{10}(T_x)$ (column (2)), normalized density $\log_{10}(\bar{\rho}_x)$ (column (3)), and normalized pressure $\log_{10}(\bar{P}_x)$ (column (4)), respectively.[2] For the $f_{SN}\,0.01$ and $f_{SN}\,0.1$ runs that do not form multiphase gas (i.e., $M_{cold}/M_{tot} < 0.01$ at all times), we present the snapshots at $t = t_{end}$, whereas we show the snapshots at $t = t_{mp}$ for the $f_{SN}\,0.5$ and $f_{SN}\,0.99$ runs.

Among the single-phase runs ($f_{SN}\,0.01$ and $f_{SN}\,0.1$), we find that the density of the gas decreases with increasing f_{SN}. The gas is also hotter. Since the SN Ia rate is fixed throughout the course of the simulation unlike the shell-by-shell heat prescription (which self-adjusts to a $(1 - f_{SN})$ fraction of the total cooling rate at each time step), whenever the net cooling rate falls below the initial cooling rate the system overheats. The amount of overheating increases with increasing f_{SN}.

Higher SN Ia rates are also associated with larger density and pressure fluctuations. This is because the SNRs are small (a few $\times 10$ parsec-scale regions) and get overheated compared to the remainder of the ISM. The overheated regions expand and rise buoyantly (as can be seen in Figure 3) and drive sound waves in the ISM. As these bubbles interact with the ISM, they form mushroom-shaped clouds characteristic of the Rayleigh–Taylor instability and drive turbulence in the ISM. The amplitudes of density and pressure fluctuations increase with increasing f_{SN}, as can be seen in the right two panels of Figure 2.

In snapshots of the multiphase runs ($f_{SN}\,0.5$ and $f_{SN}\,0.99$), we observe dense small-scale clouds that correspond to gas at or below the cooling cutoff temperature ($T \lesssim 10^{4.2}$ K). These clouds are not in hydrostatic equilibrium with the ambient ISM and rain down to the bottom of the box, forming a trail along the direction of gravity. The structure and distribution of cold gas in SN-driven turbulence are quite different from that of the cold clouds in turbulence driven on large box scales studied in M23 (see their Figure 1). In our simulations, the clouds are not volume filling (in contrast to their natural driving runs) and do not form large, box-scale filaments (in contrast to their compressive driving runs).

[2] Here, $\bar{\rho} = \rho/\langle\rho\rangle_z$, where $\langle\rho\rangle_z$ is the average ρ in a z-shell, similarly $\bar{P} = P/\langle P\rangle_z$.

Table 1
Simulation Parameters and Volume-averaged Quantities for Different Runs

Label	n_0 (cm^{-3})	H (kpc)	$\dot{N}_{SN}$ (Myr^{-1})	t_{mp} (Myr)	v ($km\ s^{-1}$)	Fr	$\mathcal{M}$	$\mathcal{M}_{comp}$	t_{ti}/t_{ff}	t_{ti}/t_{mix}	$\sigma_{s,hot}$
(1)	(2)	(3)	(4)	(5)	(6)	(7)	(8)	(9)	(10)	(11)	(12)
f_{SN} 0.01	0.08	12	0.327	>500	9.4 ± 0.1	0.40 ± 0.04	0.028 ± 0.001	0.019 ± 0.001	1.06 ± 0.01	0.78 ± 0.01	0.055 ± 0.002
f_{SN} 0.1	0.08	12	3.271	>500	15.5 ± 0.2	0.31 ± 0.03	0.041 ± 0.001	0.035 ± 0.001	1.38 ± 0.01	1.45 ± 0.05	0.114 ± 0.001
f_{SN} 0.5	0.08	12	16.35	90	26.6 ± 0.5	0.48 ± 0.03	0.071 ± 0.001	0.062 ± 0.001	1.9 ± 0.1	3.6 ± 0.32	0.204 ± 0.001
f_{SN} 0.99	0.08	12	32.39	55	33.2 ± 0.1	0.61 ± 0.03	0.088 ± 0.001	0.077 ± 0.001	3.0 ± 0.1	7.2 ± 0.2	0.306 ± 0.003
f_{SN} 0.01 hdens	0.16	12	1.212	130	11.9 ± 0.7	0.496 ± 0.001	0.036 ± 0.001	0.021 ± 0.001	0.64 ± 0.01	0.608 ± 0.001	0.115 ± 0.003
f_{SN} 0.1 hdens	0.16	12	12.12	70	18.4 ± 0.3	0.49 ± 0.01	0.054 ± 0.001	0.044 ± 0.001	0.80 ± 0.01	1.19 ± 0.01	0.200 ± 0.001
f_{SN} 0.5 hdens	0.16	12	60.59	40	30.2 ± 0.4	0.7 ± 0.1	0.086 ± 0.003	0.075 ± 0.003	1.6 ± 0.1	4.2 ± 0.2	0.36 ± 0.01
f_{SN} 0.99 hdens	0.16	12	120.0	25	36.9 ± 0.5	0.9 ± 0.1	0.103 ± 0.004	0.091 ± 0.004	2.0 ± 0.1	6.9 ± 0.3	0.43 ± 0.04
f_{SN} 0.01 ldens	0.04	12	0.077	>500	6.5 ± 0.1	0.44 ± 0.01	0.018 ± 0.001	0.014 ± 0.001	1.95 ± 0.01	1.06 ± 0.01	0.038 ± 0.001
f_{SN} 0.99 ldens	0.04	12	7.645	>500	31.46 ± 0.01	0.44 ± 0.1	0.055 ± 0.001	0.052 ± 0.001	4.5 ± 0.5	9.4 ± 0.7	0.207 ± 0.05
f_{SN} 0.01$H6$ hdens	0.16	6	1.245	>500	11.8 ± 0.3	0.445 ± 0.005	0.034 ± 0.001	0.020 ± 0.002	1.21 ± 0.02	0.67 ± 0.01	0.060 ± 0.001
f_{SN} 0.99$H6$ hdens	0.16	6	123.3	25	41 ± 1	0.73 ± 0.01	0.110 ± 0.001	0.094 ± 0.001	3.7 ± 0.3	6.7 ± 0.4	0.369 ± 0.001
f_{SN} 0.01$H3$	0.08	3	0.321	>500	11.04 ± 0.02	0.283 ± 0.001	0.032 ± 0.001	0.017 ± 0.001	3.72 ± 0.01	0.907 ± 0.002	0.044 ± 0.001
f_{SN} 0.99$H3$	0.08	3	31.79	>500	41.2 ± 0.2	0.34 ± 0.01	0.102 ± 0.001	0.089 ± 0.001	5.5 ± 0.4	4.4 ± 0.3	0.235 ± 0.005
f_{SN} 0.01$\dot{m}_*$	0.08	12	0.327	>500	8.45 ± 0.03	0.54 ± 0.04	0.028 ± 0.001	0.016 ± 0.001	1.15 ± 0.01	0.93 ± 0.01	0.062 ± 0.001
f_{SN} 0.99$\dot{m}_*$	0.08	12	32.39	40	32.4 ± 0.2	0.7 ± 0.1	0.088 ± 0.002	0.077 ± 0.001	2.69 ± 0.05	6.88 ± 0.05	0.315 ± 0.005

Notes. Column (1) shows the simulation label. The number following f_{SN} denotes the ratio of the SN energy injection rate to the net cooling rate at $t = 0$. The default initial number density n_0 is set to 0.08 cm^{-3} unless specified as hdens with $n_0 = 0.16$ cm^{-3} or ldens with $n_0 = 0.04$ cm^{-3}, respectively, and are listed in column (2). The runs with $\dot{m}_*$ in the label include mass and energy injection into the ISM by AGB winds. In column (3), we show the density/pressure scale height H, which is set to 12 (=12 kpc) for most of our runs (H is denoted in the simulation label otherwise). We list $\dot{N}_{SN}$, the total number of SNe injected in the simulation per megayear in column (4). In column (5), we show the multiphase gas formation time t_{mp} (>500 if the gas in the simulation remains in a single phase). We show mass-weighted volume averages of the standard deviation of velocity v in column (6) and dimensionless turbulence properties—the Froude number Fr, the Mach number $\mathcal{M}$, and the compressive component of the Mach number $\mathcal{M}_{comp}$ in columns (7)–(9), respectively. In columns (10) and (11), we list the ratio of thermal instability growth timescale t_{ti} to the freefall timescale t_{ff} and the turbulent mixing timescale t_{mix}, respectively. Finally, we show the amplitude of logarithmic density fluctuations in the hot phase in column (12). All averaged quantities/statistics (columns (6)–(12)) are calculated for gas with $10^6\ K \leqslant T \leqslant 3 \times 10^7$ K within the inner cube ($|x|, |y|, |z| \leqslant 0.5$), and averaged over a 15 Myr duration before t_{mp} (or t_{end} if $t_{mp} > t_{end} = 500$ Myr).

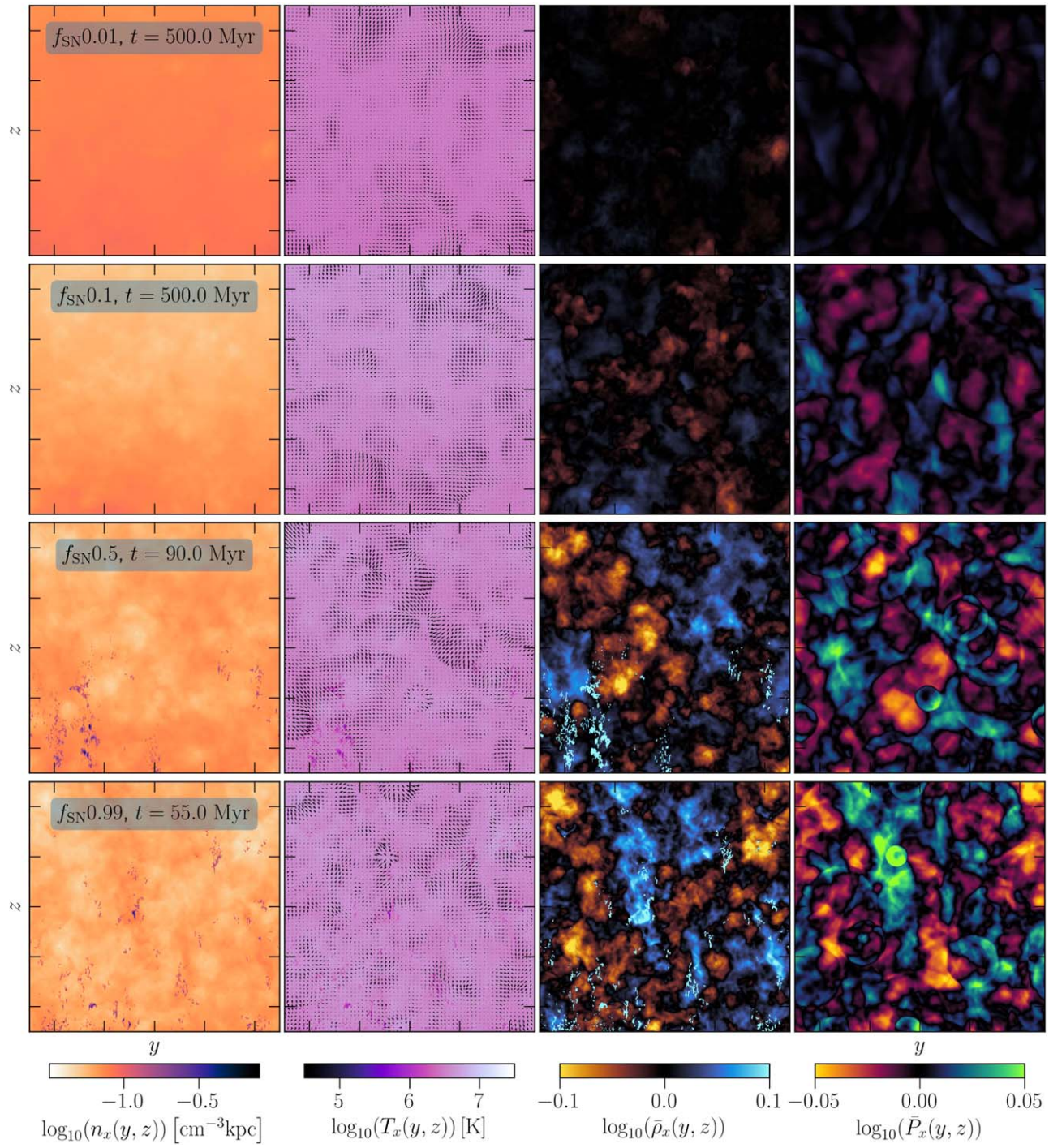

Figure 2. Snapshots of x-projected quantities for our fiducial set of simulations with different fractions of heating due to SNe at $t = t_{mp}$ ($t = t_{end}$ for f_{SN} 0.01 and f_{SN} 0.1 runs that do not form multiphase gas). Column (1): logarithm of gas number density n; column (2): Logarithm of mass-weighted temperature T, column (3): logarithm of x-projected density normalized by the z-profile of density; column (4): logarithm of x-projected pressure normalized by the z-profile of pressure. The runs with larger f_{SN} show larger density and pressure fluctuations and are more likely to undergo multiphase condensation. The cold gas forms in small dense clumps.

4.2. Time Evolution

Here, we present the time evolution of some key properties of our fiducial set of simulations. In rows 1–4 of Figure 4, we show the time evolution of net mass and energy (normalized to their values at $t = 0$), the amplitude of velocity dispersion of hot gas ($\sigma_{v,hot}$), and the mass fraction of cold gas (M_{cold}/M_{tot}), respectively. We first discuss the evolution of these quantities at initial times ($t < 100$ Myr).

We find that the net mass decreases (almost monotonically) as a function of time. The mass-loss rate increases with increasing f_{SN}. The net energy also shows a similar behavior, although the energy loss rate is much smaller and the decrease is not monotonic. We observe a clear effect of different SN Ia rates on $\sigma_{v,hot}$, where the runs with larger SN Ia rates drive stronger motions in the ISM. This is consistent with the velocity measured in observed Hα filaments on 100 pc scales in Li et al. (2020c). However, the cold and hot phases are not

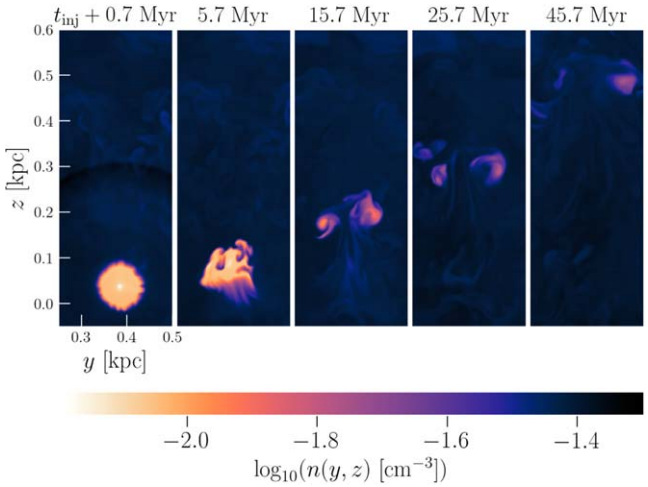

Figure 3. Snapshots of x-slices of the gas number density showing the evolution (from left to right) of an SN-inflated bubble in one of our simulations. The sound wave driven by the SN can be seen in the first column. The underdense bubble rises buoyantly and gets disrupted due to the Rayleigh–Taylor instability. These motions drive turbulence in the ISM.

comoving in our simulations. The condensed cold gas exits our simulation domain before it becomes entrained in the hot phase, so it does not trace the velocity structure of the hot phase.

Only the $f_{\rm SN}\,0.5$ and $f_{\rm SN}\,0.99$ runs trigger multiphase condensation.[3] The cold gas mass fraction shows an initial increase, followed by a steep decrease. The fraction drops below 10^{-4} in roughly $t_{\rm ff}\approx 80$ Myr after its peak value as the cold gas rains down through the bottom of the box.

The $f_{\rm SN}\,0.99$ run converts a larger fraction of its mass into the cold phase at an earlier time compared to the $f_{\rm SN}\,0.5$ run. This is because the higher SN Ia rate generates stronger density fluctuations where the dense regions cool faster, so the threshold $t_{\rm ti}/t_{\rm ff}$ for the simulation to remain single phase is higher (Choudhury et al. 2019; Voit 2021 M23).

By $t = 500$ Myr, the net mass and energy reach a rough steady state and show a slow decrease with time. Their values are smaller for larger $f_{\rm SN}$ runs since they lose more gas due to multiphase condensation as well as to outflows (which we will show in the next section). The motions in the hot phase have roughly the same $\sigma_{v,\rm hot}$ as the initial times. The system remains in a single phase after the initial round of multiphase condensation.

4.3. Mass Injection by SN Ia and Boundary Fluxes

SNe Ia inject both mass and metals into the ISM. In addition to forming metals during the SN Ia explosions, the wind driven by the SN Ia can transport these metals to the outer regions of the galaxy/into the CGM/ICM (Tang et al. 2009b). Accounting for the contribution from SN Ia is important to explain the observed radial trends of metallicity in galaxy clusters, especially for the observed amounts of Fe and Ni (Gatuzz et al. 2023a, 2023b).[4]

Here, we discuss the evolution of the mass fluxes and sources. The relevant sources/sinks of mass are the mass

[3] We define a system to be multiphase if $M_{\rm cold}/M_{\rm tot} \geqslant 0.01$ at any time, and $t_{\rm mp}$ as the first time that this criterion is satisfied.

[4] We do not evolve the metallicity of the gas in the present study and leave such a study to future work.

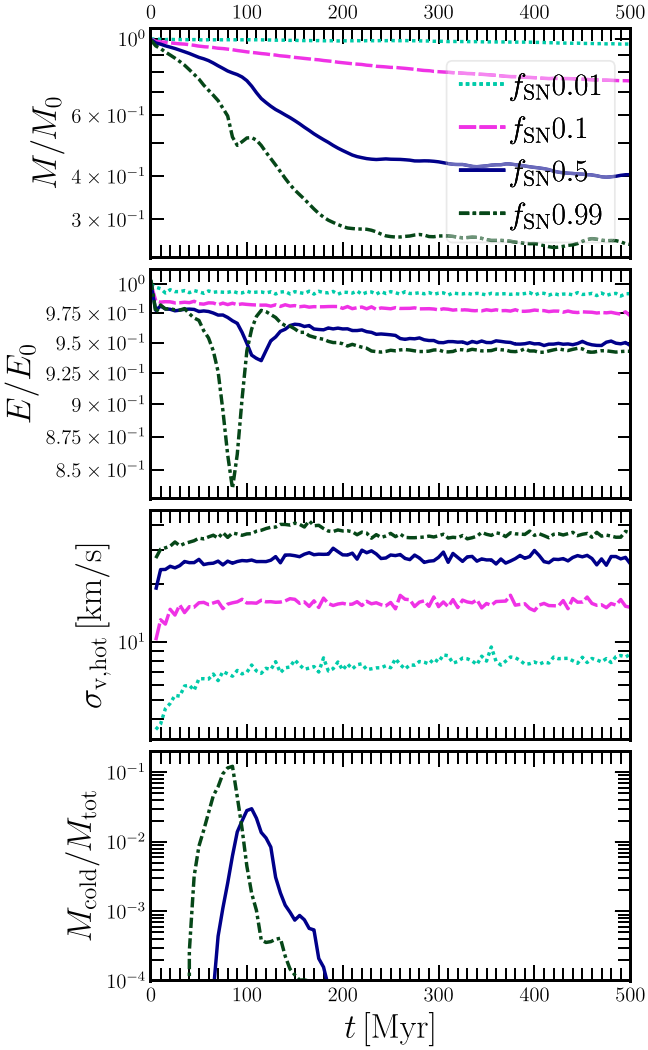

Figure 4. Time evolution of net mass (first row), energy (second row) normalized to their initial values, velocity dispersion ($\sigma_{v,\rm hot}$, column (3)) of hot gas ($T \gtrsim 10^{5.5}$ K), and mass fraction of cold gas ($T \lesssim 10^{4.2}$ K, column (4)) for our fiducial set of simulations. A higher SN Ia rate (larger $f_{\rm SN}$) leads to a larger $\sigma_{v,\rm hot}$. Stronger driving triggers multiphase condensation in the $f_{\rm SN}\,0.5$ and $f_{\rm SN}\,0.99$ runs. Imbalanced heating due to SN Ia also gives rise to wind. In a steady state, the mass and energy within the box decrease with increasing $f_{\rm SN}$ due to the increasing impact of these two processes.

outflow rate $\dot{M}_{\rm out}$, and the mass injection due to the SNe. They are defined as

$$\dot{M}_{\rm out} = \int \rho v_z\, dx dy \tag{7a}$$

$$\dot{M}_{\rm SN} = \int \dot{n}_{\rm SN} M_{\rm SN}\, dV. \tag{7b}$$

In Figure 5, we show the evolution of $\dot{M}_{\rm out}$ at the upper z-boundary $\dot{M}_{\rm out,upp}$ (row 1) and the lower z-boundary $\dot{M}_{\rm out,low}$ (row 2), respectively. In the third row, we present the mass injection rate due to the SN Ia remnants $\dot{M}_{\rm SN}$ (row 3). All mass fluxes are divided by M_0, the total mass at $t = 0$.

The mass injected due to the SN Ia remnants is dependent on $f_{\rm SN}$ as it sets the SN Ia rate. However, its value is an order of magnitude (or more) lower than the mass fluxes at the boundaries and $M_0/\dot{M}_{\rm SN} \ll 500$ Myr. So $\dot{M}_{\rm SN}$ is too small to have a significant impact on the gas density during the course of a simulation. On the other hand, $M_0/\dot{M}_{\rm out,upp}$ and $M_0/\dot{M}_{\rm out,low}$ range between 80 and 500 Myr for $f_{\rm SN} \geqslant 0.5$ and thus affect

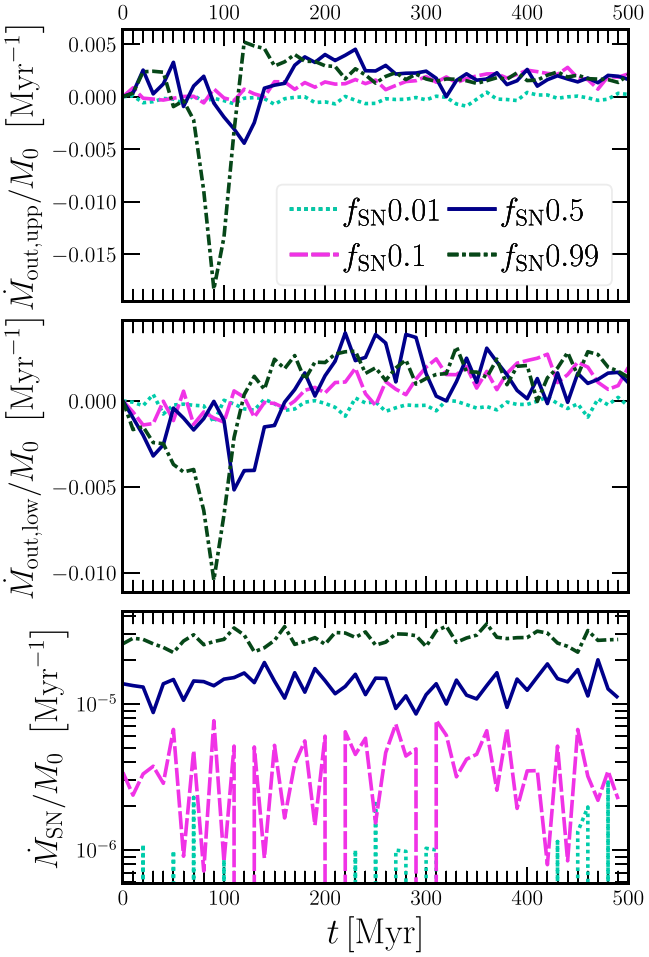

Figure 5. Time evolution of the mass fluxes at $z = 0.5$ (upp, first row) and $z = -0.5$ (low, second row) and the SN mass injection rate ($\dot{M}_{\rm SN}$, third row) for our fiducial set of simulations. The mass fluxes at the domain boundaries are an order of magnitude larger than the mass injected by the SN Ia, even for the $f_{\rm SN}\,0.99$ run. Thus, gas inflow/outflow at the boundaries dominates the evolution of net mass.

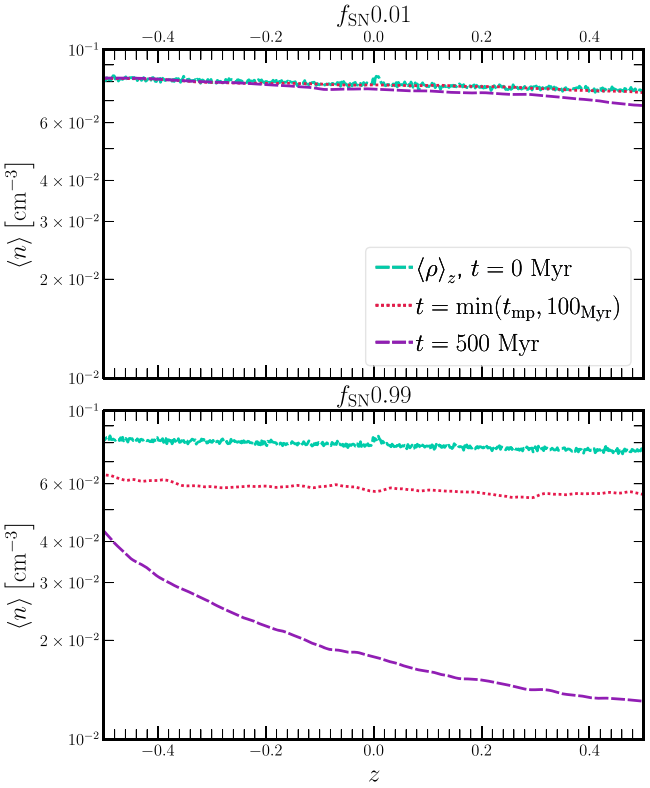

Figure 6. The z-profile of the number density of gas with $10^6\ {\rm K} < T < 10^{7.5}$ K at $t = 0$ Myr, $t = \min(t_{\rm mp}, 100\ {\rm Myr})$, and $t = 500$ Myr. Increasing the SN Ia rate leads to multiphase condensation and a strong outflow at late times. These factors contribute to a drop in n_0 as well as a change in its functional form by 500 Myr.

the overall mass distribution significantly during the course of a simulation.

Before the formation of multiphase gas at $t = t_{\rm mp}$, $\dot{M}_{\rm out,upp}$ is positive and $\dot{M}_{\rm out,low}$ is negative for the $f_{\rm SN}\,0.5$ and $f_{\rm SN}\,0.99$ runs, implying that the system is losing mass due to outflows even before multiphase condensation. At $t = t_{\rm mp}$, we observe a sharp, correlated dip in $\dot{M}_{\rm out,upp}$ and $\dot{M}_{\rm out,low}$ for both runs, which indicates cold gas raining down and hot gas flowing in from the upper boundary to replace it. This is also associated with a sharp decrease in the net mass and energy of the box. The amplitude of this drop is larger for the larger $f_{\rm SN}$ run, which forms more cold gas.

The $f_{\rm SN}\,0.01$ run does not show strong outflows or inflows at any given time. The evolution of the $f_{\rm SN}\,0.1$ runs is similar to the late-time evolution of the $f_{\rm SN}\,0.5$ and $f_{\rm SN}\,0.99$ runs, where most of the material is flowing in the positive z-direction with a similar outflow rate.

4.4. Vertical Profile of Density

In Figure 6, we show the vertical profiles of the shell-averaged number density $\langle n\rangle$ for the $f_{\rm SN}\,0.01$ and $f_{\rm SN}\,0.99$ runs from the fiducial set at $t = 0$, $\min(t_{\rm mp}, 100\ {\rm Myr})$ and $t_{\rm end}$. At $t = 0$, the squiggles in the profiles are due to the seed white noise of amplitude $\sigma_s = 0.2$ that we add. By $t = \min(t_{\rm mp}, 100\ {\rm Myr})$, we find that $\langle n\rangle$ drops while maintaining a similar dependence with z, as a result of the weak outflows driven at early times. We also note that most of the small-scale perturbations have disappeared, likely due to viscous dissipation.

By $t = t_{\rm end}$, stronger outflows in $f_{\rm SN}\,0.99$ run lead to a further drop in $\langle n\rangle$. The number density profile is also steeper. This implies that SN Ia heating drives an outflow, which can affect both the total amount of gas in the ISM and its radial distribution. So the gas density profiles found in observations (e.g., Werner et al. 2012, 2014) can evolve with time due to heating by the SN Ia.

4.5. Energy Sinks, Sources, and Boundary Flux

The heat injected by the SN Ia is highly anisotropic on small $\sim$10 pc scales, where overheated remnants are expected to rise buoyantly and drive a convective flow. Further, the SN Ia rate does not depend on the net cooling rate unlike the AGN feedback loop, where the cooling and heating are expected to be coupled through a delayed cycle (Prasad et al. 2015; Tremblay et al. 2018). Although the injection of energy due to SN Ia and the radiative cooling rate are of similar magnitude (see Figure 1), no local equilibrium is possible: SN over/underheat the ISM when the net cooling rate increases or decreases. During episodes of weaker cooling, the energy injected by the SN Ia powers an outflow, at least on the scale of our local box.

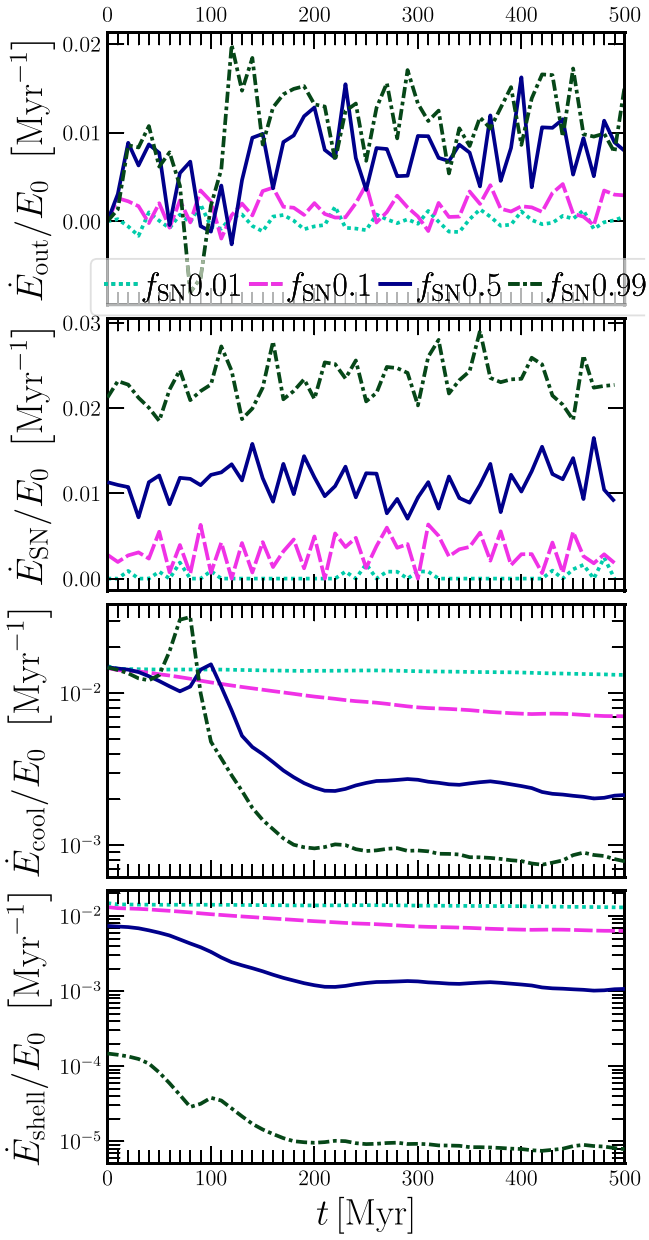

Figure 7. Time evolution of the energy outflow flux $\dot{E}_{out}$ (first row), the SN Ia energy injection rate $\dot{E}_{SN}$ (second row), radiative cooling rate $\dot{E}_{cool}$ (third row), and the shell heating rate $\dot{E}_{shell}$ sources and sinks for our fiducial set of simulations. At the initial times, the SN energy input compensates for the net cooling and drives a weak outflow. Once the cooling rate drops (after multiphase condensation), the SN Ia powers a stronger outflow.

We define the energy outflow rate $\dot{E}_{out}$ and the net energy injection/loss rate densities below[5]:

$$\dot{E}_{out} = \int \rho v_z \left(v^2/2 + \frac{\gamma}{\gamma - 1} P/\rho \right) dxdy, \tag{7c}$$

$$\dot{E}_{SN} = \int \dot{e}_{SN} dV = \int \dot{n}_{SN} E_{SN} dV, \tag{7d}$$

$$\dot{E}_{cool} = \int \mathcal{L} dV = \int n^2 \Lambda(T) dV, \text{ and} \tag{7e}$$

$$\dot{E}_{shell} = \int \dot{e}_{shell} dV. \tag{7f}$$

In Figure 7, we present the evolution of the net outflowing energy flux ($\dot{E}_{out,upp} - \dot{E}_{out,low}$) (first row), $\dot{E}_{SN}$ (second row), $\dot{E}_{cool}$ (third row), and $\dot{E}_{shell}$ (fourth row). All quantities are normalized by E_0, the net energy at $t = 0$. All the fluxes, source, and sink terms are significant during the course of a simulation (i.e., $E_0/\dot{E} \lesssim 500$ Myr). By construction, the energy injection rate due to the SN Ia increases with increasing f_{SN} and does not show much variation with time.

Before $t = t_{mp}$, we observe a net energy outflow at the boundaries. Around $t = t_{mp}$, $\dot{E}_{out}$ is briefly negative for the $f_{SN}\,0.99$ run, possibly because cold gas exits the box from the bottom and hot gas enters from the top at this time. At late times, $\dot{E}_{out}$ is positive and increases with increasing f_{SN}, with an amplitude comparable to the SN Ia heating rate.

Since the cooling rate is proportional to the square of the gas density, its evolution follows a similar trajectory as the evolution of net mass shown in Figure 4, barring the peak in the cooling rate at $t = t_{mp}$. The shell-by-shell heating rate is the $(1 - f_{SN})$ fraction of the radiative cooling losses at all times except for $t_{mp} \lesssim t \lesssim t_{mp} + t_{ff}$ in the $f_{SN}\,0.5$ and $f_{SN}\,0.99$ runs because it only replenishes cooling losses for gas with $T \gtrsim 10^{5.5}$ K (see Equation (5f)). Hence, the absence of a peak in the net $\dot{E}_{shell}$ corresponds to the formation of gas at intermediate and low temperatures ($T \lesssim 10^{5.5}$ K).

For the $f_{SN}\,0.01$ and $f_{SN}\,0.1$ runs, $\dot{E}_{SN}$ and $\dot{E}_{out}$ are much smaller compared to the cooling and shell-by-shell heating rates at all times. For the two multiphase runs ($f_{SN}\,0.5$ and $f_{SN}\,0.99$), we find that at $t \lesssim t_{mp}$, the cooling rate has an amplitude similar to that of the SN Ia heating rate and is larger than the outflow rate. However, at late times, the cooling rate drops significantly due to mass loss and most of the energy injected by the SN Ia is accounted for by a larger $\dot{E}_{out}$.

4.6. Vertical Profiles of Energy Fluxes

Here, we present the contribution of different flux components to the net energy flux at different z-shells. This is important to understand the mechanism through which SNe transfer their energy to the ISM as compared to the heat transfer mechanism by AGN (see, e.g., Tang & Churazov 2017; Bambic & Reynolds 2019; Choudhury & Reynolds 2022; Wang & Yang 2022).

The total energy flux $\dot{E}_{out}$ defined in Equation (7c) can be decomposed into different physical components, including wind (advective), convective, and wave as follows (see Parrish et al. 2009, for a similar analysis):

$$\dot{E}_{wind} = \int dxdy \langle \rho v_z \rangle \left(\underbrace{\frac{1}{2} \langle v^2 \rangle}_{\text{kin}} + \underbrace{\frac{\gamma}{\gamma - 1} \langle P/\rho \rangle}_{\text{therm}} \right), \tag{7g}$$

$$\dot{E}_{conv} = \int dxdy \frac{\gamma}{\gamma - 1} k_B \times (\langle n \rangle \langle \delta v_z \delta T \rangle + \langle v_z \rangle \langle \delta n \delta T \rangle), \tag{7h}$$

$$\dot{E}_{wave} = \int dxdy \langle \delta P \delta v_z \rangle, \tag{7i}$$

where $\langle\rangle$ represents the average over a z-shell and the fluctuations such as δn are defined as $n - \langle n \rangle$ for each shell. We break down this discussion into two subsections—(1) at

[5] Note that we have ignored Φ from our energy flux calculations because our fiducial runs have weak stratification ($H = 12$) and its contribution to the total energy is small.

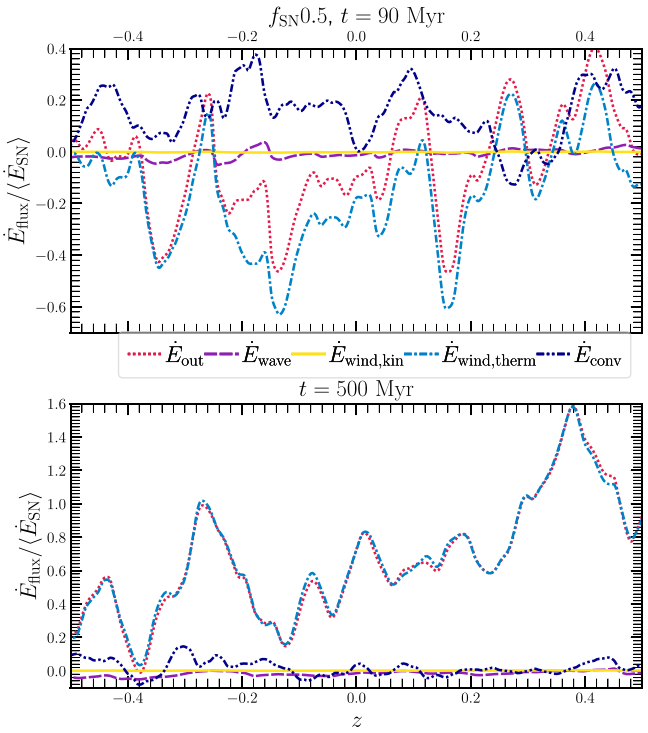

Figure 8. Vertical profiles of energy fluxes for the $f_{SN0.5}$ run at $t = t_{mp}$ (upper panel) and $t = t_{end}$ (lower panel), normalized by the mean SN Ia rate over the entire volume. Convection and thermal wind flux are the two main contributors to the net energy flux at early times. At late times, the net energy flux is mostly positive and dominated by the thermal wind flux.

early times ($t \lesssim \min(t_{mp}, 100\,\mathrm{Myr})$), shown in the upper panel of Figure 8 and (2) at $t = t_{end}$, shown in the lower panel. Since the evolution of the z-profiles of the energy fluxes does not vary much across the fiducial set, we present our analysis for the $f_{SN}\,0.5$ run only.

For $t = t_{mp}$ (or at $t = 100\,\mathrm{Myr}$), we find that the net energy flux is dominated by the contribution of the thermal wind flux. The contribution of the kinetic wind flux is low, which is expected since $\dot{E}_{wind,kin}/\dot{E}_{wind,therm} = (\gamma - 1)\mathcal{M}^2/2$ and $\mathcal{M} \lesssim 0.1$ for all our simulations (see column (8) in Table 1). The flux due to convection is also generally positive since the SNRs are overheated compared to their surroundings and rise due to buoyancy ($\delta T \times \delta v_z > 0$).

Tang & Churazov (2017) show that for an outburst in a uniform medium under spherical symmetry, the fraction of energy carried away by sound waves is $\lesssim$12%. Bambic & Reynolds (2019) showed that this fraction could be larger if a cocoon of shocked plasma generates small-scale waves, boosting their fraction to ∼25%. We do not find much energy in the form of sound waves, except small bumps in their z-profiles, which likely correspond to recently injected SN Ia. On average, the energy flux fraction in sound waves is $\lesssim$1% of $\dot{E}_{SN}$.

At $t = t_{end}$ (the lower panel of Figure 8), we find the total energy flux $\dot{E}_{tot}$ is positive at all z-shells for $f_{SN} \geqslant 0.1$, implying an outflow in the positive z-direction. It is completely dominated by the contribution of the thermal wind flux. Since the system loses mass due to outflows or condensation, the gas density decreases as a function of time; hence, $\dot{E}_{conv}$ becomes weaker at late times.

4.7. Distribution Functions

In Figure 9, we present the mass-weighted probability distribution functions (PDFs) of gas number density (column (1)), temperature (column (2)), and Mach number (column (3)). These help us understand the general characteristics of turbulence driven by SNe in a low-density ISM. All the PDFs are averaged over 10 Myr before $\min(t_{mp}, t_{end})$.

The two single-phase runs show a single peak, corresponding to the hot phase. The two multiphase runs show two distinct peaks, corresponding to the hot and cold phases, respectively. Unlike large-scale driven turbulence, the gas density distribution is not lognormal. The $f_{SN}\,0.01$ and $f_{SN}\,0.1$ runs show a low-density tail and a corresponding high-temperature tail in the temperature PDF, which are likely associated with gas inside the hot bubbles directly heated by the remnants. The gas motions in the hot phase are subsonic, with a peak of $\mathcal{M} \lesssim 0.1$ for all runs. The cold phase in the $f_{SN}\,0.5$ and $f_{SN}\,0.99$ runs is mildly supersonic, with $\mathcal{M} \sim 2$–3.

With increasing f_{SN}, the density and temperature PDFs become broader, and the peak $\mathcal{M}$ increases—denoting stronger turbulence driven by a higher SN Ia rate. We also find more gas at intermediate temperatures ($10^{4.2}\,\mathrm{K} \lesssim T \lesssim 10^{5.5}\,\mathrm{K}$). The hot, intermediate, and cold phases are observed to coexist in filaments of the M87 galaxy, with temperatures ranging from 100–10^7 K (Werner et al. 2013; Anderson & Sunyaev 2018). Since the intermediate temperature gas cools fast and has a short expected lifetime, turbulent mixing with the hot phase is one of the mechanisms proposed to continuously generate them. Heating of the cold regions (at $T \lesssim 10^4$ K) by the SN Ia and condensation from the dense regions of the hot phase can also generate gas at these intermediate temperatures. Although the filaments in M87 are likely associated with gas uplifted by the AGN jet, the SN Ia can play a role in producing gas at these temperatures through the above processes.

4.8. Density–Temperature Phase Diagram

Here, we discuss the effects of SN Ia driving on the density–temperature phase diagram. The different trend lines shown in the plots are useful for tracking the nature of the thermodynamic perturbations in the gas. The phase diagrams let us distinguish between different physical mechanisms that are responsible for energy transfer in the ISM—for example, adiabatic fluctuations can be due to compressive turbulence and sound waves, whereas isobaric fluctuations are caused by weak subsonic motions in a stratified medium (Mohapatra et al. 2020). Further, the growth rate of different modes of thermal instability t_{ti} (for example isobaric, isochoric) is expected to be different (Das et al. 2021). We can determine the relevant mode for our simulations from the phase diagram and calculate the correct t_{ti}.

In Figure 10, we show the phase diagram for the fiducial set. For the $f_{SN}\,0.5$ and $f_{SN}\,0.99$ runs, we observe the hot phase at $T \gtrsim 10^6$ K and the cold phase below the cutoff temperature at $10^{4.2}$ K. At $T \gtrsim 10^7$ K, we find adiabatic fluctuations that are likely to be associated with recently injected SNe. The perturbations in the intermediate temperature gas are mostly isobaric ($10^{4.2}\,\mathrm{K} \lesssim T \lesssim 10^{5.5}\,\mathrm{K}$). Unlike previous studies, such as that in M23, we do not observe a sharp isochoric drop at $T \sim 10^{5.5}$ K, which corresponds to the peak of the cooling curve. We note a slight steepening of the PDF at $T \sim 10^{4.5}$ K, which could be due to the under-resolution of the coldest

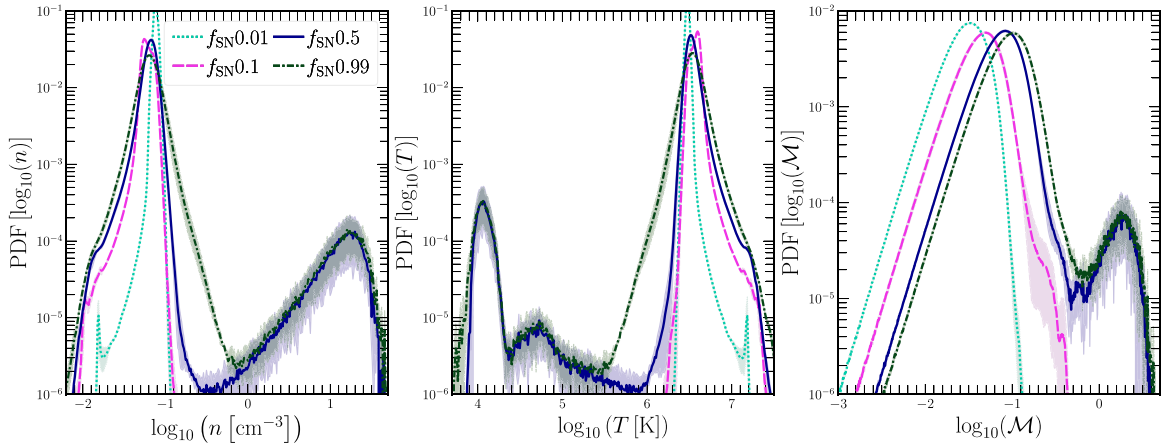

Figure 9. Mass-weighted PDFs of gas number density, temperature, and Mach number for our fiducial set at $t = \min(t_{\rm mp}, t_{\rm end})$. The two peaks in the distribution for the $f_{\rm SN}$ 0.5 and $f_{\rm SN}$ 0.99 runs correspond to the hot and cold phases. With increasing $f_{\rm SN}$, the width of the PDFs of the hot phase shows an increase, consistent with the increasing strength of turbulence.

clumps, for which we do not resolve the cooling length ($\ell_{\rm cool} = c_s t_{\rm cool}$, see Fielding et al. 2020).

With increasing $f_{\rm SN}$, we observe more contribution of adiabatic perturbations—which can be associated with compressive turbulence and sound waves directly driven by recently injected SNe. Arévalo et al. (2016) analyzed the nature of X-ray brightness fluctuations for M87 using the hardness ratio of X-ray spectra in Chandra observations (also see Zhuravleva et al. 2018). They find the filamentary regions to be isobaric, weakly shocked regions to be adiabatic and the remaining regions to be a combination of the two. Our findings suggest that the subsonic turbulence driven by the SN Ia can contribute to either of the two observed modes.

4.9. Condition for Multiphase Gas Formation Fiducial Runs

For the gas around galaxies and galaxy clusters, the ratio $t_{\rm ti}/t_{\rm ff}$ is an important criterion to determine whether a thermally unstable system forms multiphase gas (McCourt et al. 2012; Sharma et al. 2012). A small $t_{\rm ti}/t_{\rm ff}$ ($\lesssim$10) has been associated with the existence of multiphase gas in both simulations (Prasad et al. 2018) and observations (Olivares et al. 2019). More recent theoretical studies have indicated that the threshold value of $t_{\rm ti}/t_{\rm ff}$ for multiphase gas formation depends on the amplitude of density/entropy fluctuations (Choudhury et al. 2019; Voit 2021; M23).

In Figure 11, we plot the minimum value of the z-shell-averaged value of $t_{\rm ti}/t_{\rm ff}$ versus the amplitude of logarithmic density fluctuations for gas with $T > 10^6$ K. The dashed–dotted black line shows the condensation curve proposed by M23, scaled down[6] by a factor of 0.6.

We observe a clear impact of the role played by SN Ia driving on the occurrence of multiphase condensation. In the $f_{\rm SN}$ 0.01 and $f_{\rm SN}$ 0.1 runs, the seed density fluctuations at $t = 0$ are quickly damped by viscous forces, and the weak SN Ia driving does not generate large density fluctuations. As a result, the simulations no longer satisfy the condensation criterion and remain in a single phase until $t = t_{\rm end}$. The stronger SN Ia driving in the $f_{\rm SN}$ 0.5 and $f_{\rm SN}$ 0.99 runs increases the amplitude of density fluctuations. However, the larger number of injected SN Ia also drives an outflow at initial times (see Figures 5 and 7) and overheats small regions of the gas where the remnants deposit their energy. These processes decrease the gas density and as a result increase $\min(t_{\rm ti})/t_{\rm ff}$. After accounting for the combined effect of the two, the system still satisfies the condensation criterion and forms multiphase gas.

5. Effect of Varying Other Parameters and Summary

In the previous section, we discussed the effects of varying the level of SN Ia heating while keeping all other parameters constant. In this section, we vary different simulation parameters such as the mean gas density, the strength of gravity, inclusion of heating due to AGB winds, and assess the impact of switching SN Ia heating on/off in these systems. These help us understand the local effects of SN Ia heating on the ISM in different regions of early-type galaxies.

5.1. Scaling of Fluctuations with the Rms Mach Number

Observational studies of the hot gas around giant elliptical galaxies or galaxy clusters often rely on indirect techniques such as using the amplitude of surface brightness fluctuations (which are dependent on the gas density, e.g., Zhuravleva et al. 2014, 2015, 2018) or fluctuations in the thermal Sunyaev–Zeldovich effect to infer the amplitude of the turbulent gas velocities (which depend on the thermal pressure of the gas, e.g., Khatri & Gaspari 2016; Romero et al. 2023). On the other hand, direct measurements of the turbulent velocities using the high spectral-resolution telescope XRISM[7] can be used to infer the state of perturbations in the hot ISM. In this subsection, we present the scaling relation between the gas density/pressure fluctuations and the turbulent Mach number for SN Ia-driven turbulence.

In Figure 12, we show the joint evolution of $\sigma^2_{s,\rm hot}$ (row 1) and $\sigma^2_{\ln(\bar{P}),\rm hot}$ (row 2) versus $\mathcal{M}$ (column (1)) and its compressive component $\mathcal{M}_{\rm comp}$ (column (2)). The dashed lines in each panel show empirical fits to the data. The dotted line in the top right panel shows the σ_s–$\mathcal{M}_{\rm comp}$ scaling relation for homogeneous turbulence forced on large scales from Konstandin et al. (2012).

[6] There is some ambiguity in defining $t_{\rm ti}$ since the value of $d\ \ln\Lambda/dT$ changes for 10^6 K $< T < 10^7$K. Further, it is nontrivial to define the density dependence of the heating by the SN Ia ($\alpha_{\rm heat}$ parameter in Equation (6e)). We find that scaling down the M23 condensation curve by a factor of 0.6 separates the single and multiphase simulations of our study well.

[7] https://heasarc.gsfc.nasa.gov/docs/xrism/about/

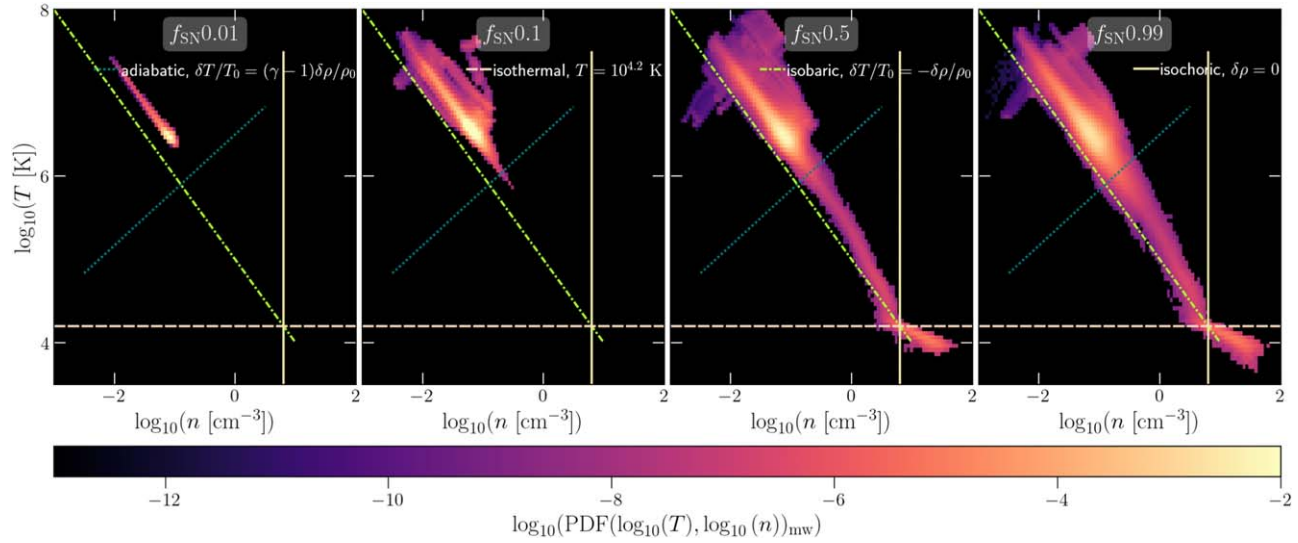

Figure 10. Phase diagram showing the joint mass-weighted distribution of the gas temperature and density (in log-scale) for our fiducial set of simulations. The perturbations in the hot phase are mostly isobaric in nature. Recently injected SNe Ia appear as adiabatic fluctuations. The peak near $T \sim 10^4$ K for "f_{SN} 0.5" and "f_{SN} 0.99 runs correspond to cold gas that has reached $T_{floor}(=10^{4.2}$ K).

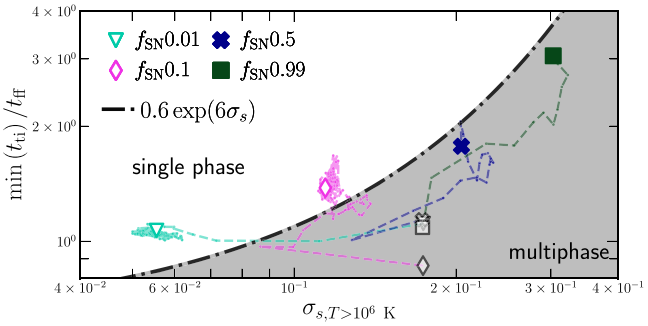

Figure 11. The time evolution of the minimum value of the ratio t_{ti}/t_{ff} plotted against σ_s for the fiducial set. The dark gray points show the value of this ratio at $t = 0$. Simulations that do not form multiphase gas are shown as unfilled colored data points at $t = t_{end}$ and simulations that form multiphase gas are shown as filled colored data points at $t = t_{mp}$. The colored dashed lines show the evolution of this ratio from $t = 0$ to $t = \min(t_{mp}, t_{end})$. The dashed–dotted trend line is a scaled version of the condensation criterion proposed in M23. Although all four simulations start with similar $\min(t_{ti})/t_{ff}$, their evolution is strongly dependent on the SN Ia rate.

In general, we find that both $\sigma_{s,hot}$ and $\sigma_{\ln(\bar{P}),hot}$ increase with increasing $\mathcal{M}$ or $\mathcal{M}_{comp}$. The amplitude of pressure fluctuations is much smaller than that of density fluctuations. The fluctuations are larger for runs with higher f_{SN}, in line with our expectations. The multiphase runs (represented by the filled markers) are typically associated with larger f_{SN} and thus are found in the top right of each panel, whereas the single-phase regions are typically found in the bottom left, with a few exceptions. Among the runs with the same f_{SN} but different densities, the ldens (hdens) runs have a lower (higher) cooling rate, and hence weaker (stronger) SN Ia driving and smaller (larger) $\sigma_{s,hot}$, $\sigma_{\ln(\bar{P}),hot}$ compared to the fiducial set. Variations in the other parameters such as H or the inclusion of stellar heating do not have any significant effect on these results.

Both $\sigma_{s,hot}$ and $\sigma_{\ln(\bar{P}),hot}$ follow power-law scaling with $\mathcal{M}$ and $\mathcal{M}_{comp}$ with some scatter around the empirical fits. We find a tight relation between $\sigma_{\ln(\bar{P}),hot}$ and $\mathcal{M}_{comp}$. Similar to MLi20b, we find both fluctuations to be much larger than predicted by scaling relations in the literature, such as in Konstandin et al. (2012) and Mohapatra et al. (2021, 2022). Unlike the proposed scaling relations, which were based on idealized turbulence driven by exciting particular modes in k-space, the SNe overheat small regions of the gas, which expand, rise buoyantly, and drive turbulence in the ISM. Heating by the SN Ia and radiative cooling of the ISM are also associated with isobaric density perturbations, as seen in Figure 10. We expect the differences between such idealized driving and SN Ia driving to be due to the heating and cooling of the gas, as well as the differences in driving scale, modes, etc.

Compared to MLi20b, who study SN Ia-driven turbulence in an unstratified box (i.e., without external gravity), we observe some key differences. The amplitude of perturbations that we observe are smaller by a factor of 4 or more compared to that of MLi20b for the same $\mathcal{M}$. This is likely due to the smaller ratio between the power in compressive and solenoidal modes in our simulations, even though the contribution from compressive modes still dominates the total power. In our simulations, we find that the bubbles inflated due to the energy deposited by the SN Ia rise buoyantly and form mushroom-shaped clouds, which are a typical characteristic of the Rayleigh–Taylor (RT) instability (see Figure 3). The motion of the hot bubble gas with respect to the ambient medium also generates Kelvin–Helmholtz (KH) instability. Both the RT and KH instabilities can drive solenoidal turbulence in the ISM and increase its contribution to the total power.

Although the amplitude of density and pressure fluctuations generated by SN Ia-driven turbulence is large, they may be difficult to detect since they occur on $\lesssim$100 pc scales. First of all, small-scale fluctuations would be canceled out due to averaging along the line of sight. Second, most current X-ray and microwave telescopes lack the resolution to resolve small scales even for nearby massive elliptical galaxies ($R_{fade} \sim 46$ pc $\sim 0\farcs5$ for the M87 galaxy, which is close to the resolution limit of the Chandra telescope). Future X-ray telescopes, such as AXIS,[8] would be useful to measure these ISM properties with their higher angular resolutions and better sensitivities. The synchrotron emission from the electrons accelerated in the

[8] https://axis.astro.umd.edu/

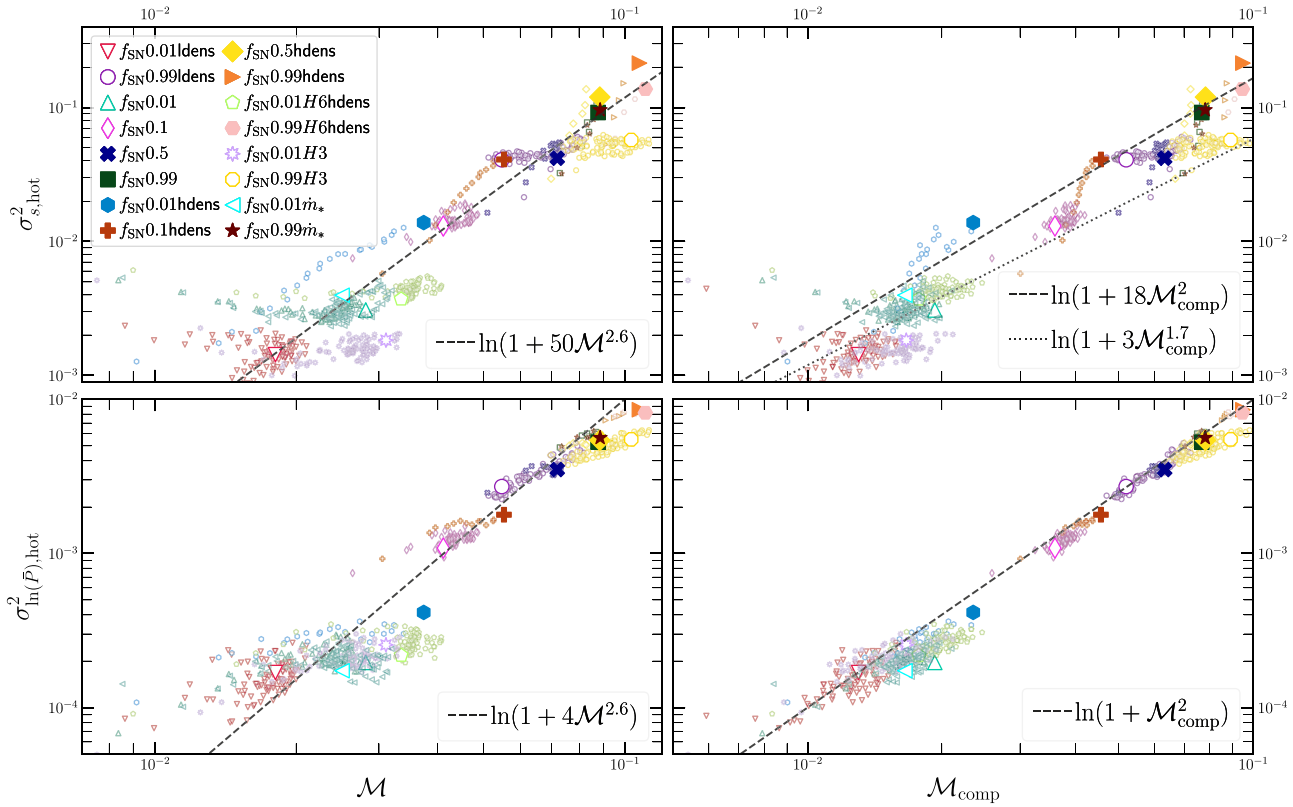

Figure 12. First row: the square of the amplitude of logarithmic density fluctuations (σ_s^2) plotted against the Mach number ($\mathcal{M}$) (left column) and its compressive component $\mathcal{M}_{\rm comp}$. The larger symbols represent the data points at $t = \min(t_{\rm mp}, t_{\rm end})$ and the smaller symbols show their values are at earlier times. The filled symbols denote simulations that form multiphase gas (right column). The dotted line on the right panel shows the predicted scaling relation for subsonic turbulence with compressive forcing from Konstandin et al. (2012). Second row: similar to the first row, but for the square of logarithmic pressure fluctuations $\sigma^2_{\ln(P/\langle P\rangle)}$ instead. The dashed lines in all four panels show our empirical fits to the data. The pressure fluctuations show a tight scaling with $\mathcal{M}_{\rm comp}$.

SN Ia shocks could be detected in radio wavelengths. However, it would be challenging to distinguish them from the radio emission from other sources, such as shocks due to AGN activity and mergers.

5.2. Condition for Multiphase Gas Formation in All Runs

In this subsection, we revisit the criteria for multiphase gas condensation for all our simulations. In addition to the $\min(t_{\rm ti})/t_{\rm ff}$ we discussed earlier, we also check the importance of turbulent mixing in suppressing multiphase condensation, as proposed by Gaspari et al. (2018).

In the first row of Figure 13, we show the ratio $t_{\rm mp}/\langle t_{{\rm ti},t=0}\rangle$ (averaged over the entire volume) versus $\sigma_{s,\rm hot}$. Seven out of our 14 simulations form multiphase gas, denoted using filled markers. We show $t_{\rm end}/\langle t_{{\rm ti},t=0}\rangle$ as the lower limit of $t_{\rm mp}/\langle t_{{\rm ti},t=0}\rangle$ for the single-phase runs, which are denoted by unfilled data points. For most of the multiphase runs, $t_{\rm mp}/\langle t_{{\rm ti},t=0}\rangle < 1$. Since the SN Ia driving generates large density fluctuations, locally dense regions cool in less than the $\langle t_{{\rm ti},t=0}\rangle$. The $f_{\rm SN}\,0.01$ hdens and the $f_{\rm SN}\,0.1$ hdens runs are the two exceptions since the SN Ia driving is weak for these runs.

In the second row, we show the ratio $\min(t_{\rm ti})/t_{\rm ff}$ versus $\sigma_{s,\rm hot}$ for all runs. The values of these two quantities at $t = 0$ are denoted by the unfilled dark gray markers and the dashed lines show their evolution with time until $\min(t_{\rm mp}, t_{\rm end})$. We start with $\sigma_{s,\rm hot} \approx 0.2$ for all runs except the hdens set, for which we set $\sigma_{s,\rm hot} \approx 0.05$. In general, we find that $\sigma_{s,\rm hot}$ decreases with time for the runs with $f_{\rm SN} = 0.01$ that remain single phase and increases with time for the runs with $f_{\rm SN} = 0.99$ that form multiphase gas. The value of $\sigma_{s,\rm hot}$ stays roughly constant for the $f_{\rm SN} = 0.99$ runs that remain in a single phase. For most of the hdens runs, $\sigma_{s,\rm hot}$ increases with time, which we associate with the onset of thermal instability.

Now we shift our focus to the values of this ratio at $t = \min(t_{\rm ti}, t_{\rm end})$, represented by the colored markers. We refer the reader to Table 1 for important simulation parameters. We find that the runs with stronger stratification ($f_{\rm SN}\,0.01H3$ and $f_{\rm SN}\,0.99H3$) do not form multiphase gas due to the shorter $t_{\rm ff}$, which increases the value of $\min(t_{\rm ti})/t_{\rm ff}$. Comparing the high-density hdens set and the fiducial set, we find that both the $f_{\rm SN}\,0.01$ hdens and $f_{\rm SN}\,0.1$ hdens runs form multiphase gas (in addition to the $f_{\rm SN}\,0.5$ hdens and $f_{\rm SN}\,0.99$ hdens runs) due to the shorter $t_{\rm ti}$. However, once we double the strength of the stratification, the $f_{\rm SN}\,0.01H6$ hdens run no longer forms multiphase gas due to a smaller $t_{\rm ff}$, whereas the $f_{\rm SN}\,0.99H6$ hdens run still does. In the ldens runs, due to the longer $t_{\rm ti}$ neither $f_{\rm SN}\,0.01$ ldens nor $f_{\rm SN}\,0.99$ ldens runs form multiphase gas. The runs with AGB winds ($f_{\rm SN}\,0.01\dot{m}_*$ and $f_{\rm SN}\,0.99\dot{m}_*$) show similar trends as their fiducial counterparts. The exponential condensation curve that we introduced in Section 4.9 separates all our single and multiphase simulations well, i.e., the final value of $\min(t_{\rm ti})/t_{\rm ff}$ is smaller (larger) than the condensation curve if the simulation forms (does not form) multiphase gas.

In the third row, we show the ratio $\min(t_{\rm ti})/t_{\rm mix}$ as a function of $\sigma_{s,\rm hot}$. We also draw an exponential curve in an attempt to separate the simulations that form multiphase gas from the ones that do not. Except for the $f_{\rm SN}\,0.99H3$ run, which has strong

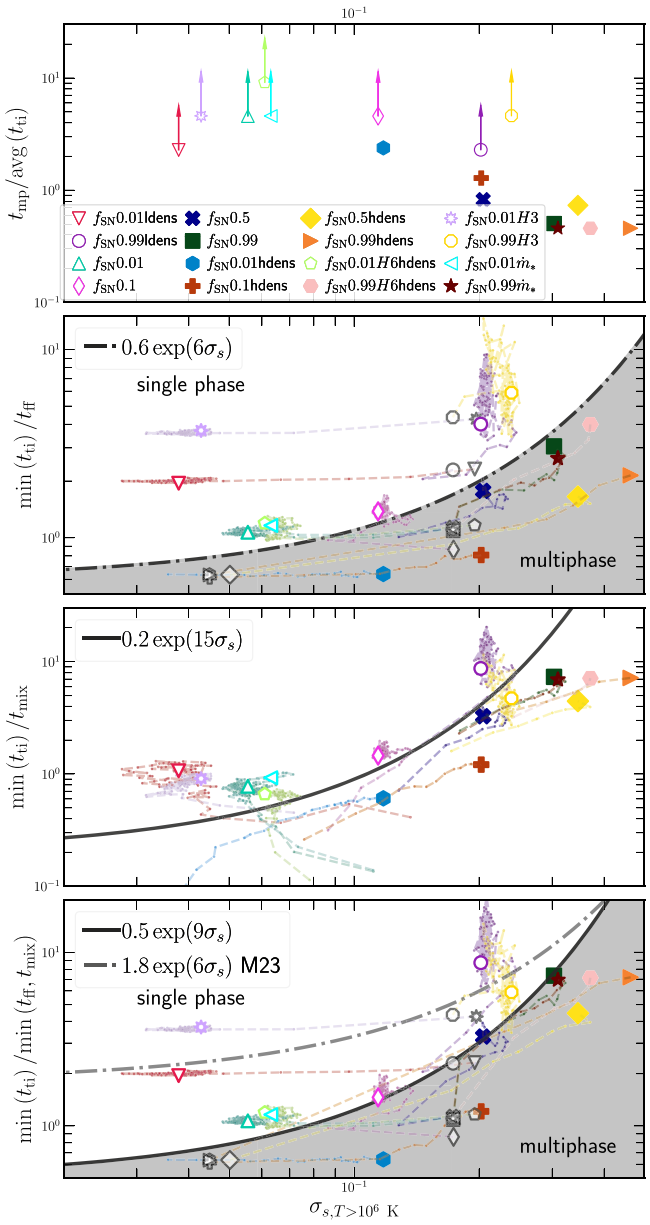

Figure 13. First row: the time taken by a simulation to form multiphase gas normalized by the initial thermal instability timescale $t_{mp}/\mathrm{avg}(t_{ti})_{t=0}$ plotted against the amplitude of logarithmic density fluctuations in the hot phase $\sigma_{s,hot}$. When the simulation forms multiphase gas, we show the data points as filled markers. When they remain single phase until $t = t_{end}$, we show the lower limit of this ratio and mark them as unfilled data points and an upward arrow. Second row: the minimum value of the ratio t_{ti}/t_{ff} plotted against σ_s. The dark gray points show the value of this ratio at $t = 0$ and the dashed lines show the evolution of this ratio until $t = \min(t_{mp}, t_{end})$. The dashed–dotted curve shows the t_{ti}/t_{ff}–σ_s condensation criterion, which separates the plot into single and multiphase regions. Third row: similar to the second row, but showing the ratio t_{ti}/t_{mix} instead. Fourth row: here, we show the larger of the two ratios shown in rows 2 and 3. The dotted–dashed line shows the condensation criterion proposed by M23. The solid line is a rescaled version of this criterion, which fits our results better.

stratification, this curve also separates between the single and multiphase simulations.

In the fourth row, we show the joint ratio $\min(t_{ti})/\min(t_{ff}, t_{mix})$, which is used to define the multiphase condensation criterion in M23. The dotted–dashed line shows the condensation curve in M23, whereas the solid line shows a rescaled version, which is a better empirical fit to the data in this work. Thus, both short t_{ff} and short t_{mix} can prevent multiphase condensation. Among our simulations with the same values of t_{ff} and initial t_{ti}, increasing f_{SN} leads to larger density perturbations. The increase in the solenoidal component of turbulence (due to the larger SN Ia rate) is generally insufficient to mix these perturbations with the ambient gas and prevent multiphase condensation.

6. Caveats and Future Work

In this section, we discuss some of the shortcomings of this study. We also outline some interesting aspects to consider in future works.

6.1. Boundary Conditions

We have modeled a small 1.5 kpc^3 patch of the ISM of an elliptical galaxy using a cuboidal box oriented along the direction of the stratification of the ISM. Our boundary conditions are outlined in detail in Section 3.2.2. We have also tested the effect of the outflow for v_z at the z-boundaries, hydrostatic equilibrium for P, and ρ or constant ratio boundary conditions. We find that the evolution of our multiphase simulations for $t > t_{mp}$ is sensitive to the choice of boundary conditions. If we do not fix the density and pressure at the upper and lower boundaries, once any cold gas forms it triggers a large-scale cooling flow and the simulation domain loses all its mass. Most of the other choices that we tested face this issue. The choice of boundary conditions does not have a significant effect on our simulations that remain in a single phase at all times.

6.2. Geometry

The hot ISM in elliptical galaxies is expected to follow an elliptical/spherical distribution, whereas we model it as a plane-parallel atmosphere. This difference in geometry can affect the energy and mass outflow rates since the hot gas is expected to expand and cool at larger radii. We plan to conduct global galaxy-scale simulations with the appropriate geometry in the future, which will let us address the fate of the SNe heated gas. This will also resolve the challenge of boundary condition sensitivity highlighted in the previous paragraph.

6.3. Heating Model

We include an additional heating term that replenishes the $(1 - f_{SN})$ fraction of the radiative losses in each z-shell. This modification also improved the stability of the atmosphere against a large-scale cooling flow. This overly idealized heating model is motivated by the observational evidence for global thermal stability in massive galaxies but in detail it cannot be correct and the formation of multiphase gas and the long-term evolution of the hot ISM may be sensitive to the details of the correct heating function.

Many massive elliptical galaxies have AGN and the AGN jets can drive large-scale motions in the ISM. The in-fall of satellite galaxies can also add mass and drive turbulence in the ISM. We have not considered their effects in this study.

6.4. Resolution

We have performed all simulations listed in Table 1 at two resolutions—$512^2 \times 768$ and $256^2 \times 384$. We find the results of our single-phase runs are convergent with increasing the

resolution. Among the multiphase runs, we find that the results diverge for $t \geqslant t_{\rm mp}$. The lower-resolution runs from more cold gas compared to their high-resolution counterparts. This may be due to the effects of excessive averaging at the boundary layers between the hot and cold regions, which forms more gas at intermediate temperatures ($10^5\,{\rm K} < T < 10^6\,{\rm K}$). The intermediate temperature gas cools fast and forms more cold gas in the lower-resolution simulations.

6.5. Physics

We have ignored the effect of important physics such as magnetic fields (Hopkins et al. 2020; Wang et al. 2021; Buie et al. 2022), cosmic rays (Butsky et al. 2020; Kempski & Quataert 2020; Beckmann et al. 2022), and conduction (Parrish et al. 2009; El-Badry et al. 2019), see Faucher-Giguère & Oh (2023) for a review. Magnetic fields and cosmic rays are expected to be energetically important and can affect the properties of the thermal energy-driven outflow. Conduction can affect the energy exchange between the SN Ia inflated bubbles and the ISM. All three can affect the formation of cold gas and its kinematics. In future studies, we plan to include some of these physical properties and study their impact.

6.6. Chemical Evolution

We have ignored the evolution of the chemical composition of the ISM due to metals injected into the ISM by the SN Ia. SNe Ia are one of the main sources of elements such as `Fe`, `Co`, `Ni`, etc. The gas cooling rate at $T \sim 10^6\,{\rm K}$ is sensitive to the chemical composition of the ISM. We plan to include heavy element injection and transport in future works and study their properties such as their radial extent, spatial variations, etc.

7. Conclusion

In this paper, we model a $1.5\,{\rm kpc}^3$ local stratified patch of the hot ISM of a massive elliptical galaxy. We study the effect of different strengths of heating due to the SN Ia, motivated by the observational fact that the SN Ia heating rate is of order the radiative cooling rate in many massive galaxies (see, e.g., Figure 1). We fix the heating rate due to the randomly injected SN Ia to a fraction $f_{\rm SN}$ of the net cooling rate of the ISM and compare the hot ISM properties against a uniform shell heating model typically used in idealized simulations. We have conducted a total of 16 simulations, where we vary ISM properties such as gas density and the strength of stratification. Here, we summarize some of our key findings:

1. The SNe Ia deposit their energy in small $\sim$20 pc size regions of the ISM. These regions expand and rise buoyantly, driving turbulence in the ISM. The turbulence is associated with large density fluctuations (Figures 2 and 3).
2. The high-density regions have a short cooling time. Since the ISM at these temperatures is thermally unstable, if the ratio of the thermal instability growth time to the freefall time ($t_{\rm ti}/t_{\rm ff}$) is small enough, the dense regions cool down to the cooling cutoff temperature at $10^{4.2}$ K, they are out of hydrostatic equilibrium and rain down through the bottom of the box. Since the SN Ia seed these density fluctuations (also seen in MLi20a), a larger SN Ia injection rate is more likely to trigger multiphase condensation (Figure 11). Much of the literature has focused on the formation of multiphase gas by thermal instability (e.g., McCourt et al. 2012; Sharma et al. 2012; Choudhury et al. 2019) or AGN-driven uplift of gas (e.g., Pulido et al. 2018; Huško & Lacey 2023). Our results show that the SNe Ia are also efficient sources of multiphase gas production in the hot ISM/ICM of massive galaxies, groups, and clusters. A spatially and temporally resolved treatment of the SNe Ia is likely critical for understanding the formation of multiphase gas in massive galaxies and its role in fueling star formation and black hole growth.
3. As the SN Ia rate is fixed, once the gas density drops due to multiphase condensation, the SNe Ia overheat the ISM and drive an outflow. The net mass remaining in the simulation decreases with increasing SN Ia rate (Figures 4 and 5). Even in the simulations that do not form multiphase gas, whenever the net heating exceeds the net cooling, the SNe Ia drive an outflow, which further decreases the net mass and the cooling rate. This evolution reflects the fact that heating by the SN Ia is inevitably unstable: unlike core-collapse SNe or (plausibly) AGN, there is no connection between the SN Ia rate and the radiative cooling of the hot gas. Global simulations will be required to understand the ultimate outcome of this instability.
4. In the initial phases of our simulations (prior to multiphase gas condensation), the total energy flux is set by the sum of convective and thermal wind fluxes, whereas sound waves and wind kinetic energy carry negligible amounts of energy. At late times, after multiphase gas condensation, the convective energy flux also drops and the wind becomes the dominant energy transport mechanism (Figure 8). Multiphase condensation and outflows also strongly alter the z-profile of gas density (Figure 6).
5. The SNe Ia drive subsonic turbulence in the ISM, which cause isobaric perturbations in it (Figures 9 and 10). The amplitudes of the density and pressure fluctuations are proportional to the compressive component of the rms Mach number. However, the fluctuations generated by the SN Ia are much larger than predicted by the density fluctuations—rms Mach number scaling relation in homogeneous turbulence (Konstandin et al. 2012), in agreement with MLi20b. We expect that these differences are due to the additional thermodynamics in our simulations, i.e., perturbations associated with the direct heating of the ISM by the SN Ia and the radiative cooling of the ISM.
6. For all 16 simulations, we find that multiphase condensation occurs if the criterion $\min(t_{\rm ti})/t_{\rm ff} \leqslant c_1 \exp(c_2 \sigma_s)$ is satisfied. We obtain $c_1 = 0.6$ and $c_2 = 6$ using an empirical fit (Figure 13). In contrast with the simulations of idealized driven turbulence in M23, we find turbulent mixing does not suppress multiphase condensation even when $t_{\rm ti}/t_{\rm mix} \gg 10$. This is because the SNe Ia drive compressive turbulence, which is poor at mixing perturbations in the gas. Thus, one needs to be careful in interpreting the importance of $t_{\rm ti}/t_{\rm mix}$ in observations, where it is difficult to determine the source/driving mode of turbulence.

Acknowledgments

R.M. would like to thank Minghao Guo, Patrick Mullen, and Jim Stone for help with setting up the simulations using

Athenak and post-processing the results. We thank Chang-Goo Kim, Prateek Sharma, Romain Teyssier, and Eve Ostriker for useful discussions. We thank the anonymous referee for the comments, which helped improve this paper. This work was supported in part by a Simons Investigator award from the Simons Foundation (EQ) and by NSF grant AST-2107872. The analysis presented in this article was performed in part on computational resources managed and supported by Princeton Research Computing, a consortium of groups including the Princeton Institute for Computational Science and Engineering (PICSciE) and the Office of Information Technology's High Performance Computing Center and Visualization Laboratory at Princeton University. We also used the Delta GPU machine at the National Center for Supercomputing Applications, Illinois, United States through allocations PHY230106 and PHY230045 from the Advanced Cyberinfrastructure Coordination Ecosystem: Services and Support (ACCESS) program, which is supported by National Science Foundation grants 2138259, 2138286, 2138307, 2137603, and 2138296. The Delta research computing project is supported by the National Science Foundation (award OCI 2005572), and the State of Illinois. Delta is a joint effort of the University of Illinois at Urbana-Champaign and its National Center for Supercomputing Applications.

Software: `Athena++` (Stone et al. 2020), `matplotlib` (Hunter 2007), `cmasher` (van der Velden 2020), `SciPy` (Virtanen et al. 2020), `NumPy` (Harris et al. 2020), `CuPy` (Okuta et al. 2017), `h5py` (Collette 2013) and `astropy` (Astropy Collaboration et al. 2018).

Data Availability

All relevant data associated with this article is available upon reasonable request to the corresponding author.

Additional Links

Movies of density, temperature, density fluctuations, and pressure fluctuations along slices at $x = 0$ are available at the following links:

1. Fiducial runs: https://youtu.be/EhY205ezfsU
2. hdens runs: https://youtu.be/xXRj2j7zrYE
3. ldens runs: https://youtu.be/LHbx7Cp2mkE
4. *H6*hdens runs: https://youtu.be/_Ti4wZ0F_x8
5. *H3* runs: https://youtu.be/nlyCZBC_Krs
6. $\dot{m}_*$ runs: https://youtu.be/xNnO2jJZHmM.

Appendix
Effect of Including AGB Winds

In Section 2.1.4, we discussed that the energy injected into the ISM due to the thermalization of the material ejected by AGB stars can contribute to its heating. The mass injected by these stars can also change the density of the ISM and its cooling rate. We have described our implementation of mass and energy input due to AGB wind ejecta in Section 3.3.3. Here, we study their effect on the time evolution of important parameters in our simulations.

In Figure A1, we show the evolution of the net mass, net energy, hot gas dispersion velocity, and mass fraction of cold gas for our fiducial $f_{\rm SN}\,0.99$ run and the $f_{\rm SN}\,0.99\dot{m}_*$ run. Comparing the two, we do not find any major differences. We do observe that the net mass in the $f_{\rm SN}\,0.99\dot{m}_*$ run increases slowly at late times, possibly due to mass injection from the AGB winds. The additional mass in the system raises the gas density and is also responsible for the formation and existence of cold gas in the simulation domain until $\sim$250 Myr, compared to 150 Myr for the $f_{\rm SN}\,0.99$ run.

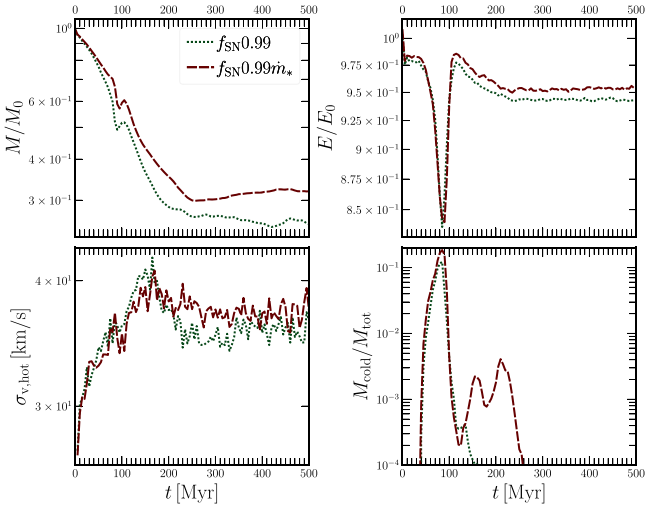

Figure A1. Time evolution of net mass (row 1, column (1)), energy (row 1, column (2)), velocity dispersion of hot gas (row 2, column (1)), and mass fraction of cold gas (row 2, column (2)) for our fiducial $f_{\rm SN}\,0.99$ run and the $f_{\rm SN}\,0.99\dot{m}_*$ run implementing mass and injection of energy from AGB winds. We find no major differences between the two, except a larger fraction of cold gas formation for the $f_{\rm SN}\,0.99\dot{m}_*$ run.

ORCID iDs

Rajsekhar Mohapatra https://orcid.org/0000-0002-1600-7552
Eliot Quataert https://orcid.org/0000-0001-9185-5044

References

Allen, S. W., Dunn, R. J. H., Fabian, A. C., Taylor, G. B., & Reynolds, C. S. 2006, MNRAS, 372, 21
Anderson, M. E., & Sunyaev, R. 2018, A&A, 617, A123
Arévalo, P., Churazov, E., Zhuravleva, I., Forman, W. R., & Jones, C. 2016, ApJ, 818, 14
Astropy Collaboration, Price-Whelan, A. M., Sipőcz, B. M., et al. 2018, AJ, 156, 123
Bambic, C. J., & Reynolds, C. S. 2019, ApJ, 886, 78
Barkhudaryan, L. V., Hakobyan, A. A., Karapetyan, A. G., et al. 2019, MNRAS, 490, 718
Beckmann, R. S., Dubois, Y., Pellissier, A., et al. 2022, A&A, 665, A129
Bîrzan, L., Rafferty, D. A., McNamara, B. R., Wise, M. W., & Nulsen, P. E. J. 2004, ApJ, 607, 800
Buie, E., Scannapieco, E., & Mark Voit, G. 2022, ApJ, 927, 30
Butsky, I. S., Fielding, D. B., Hayward, C. C., et al. 2020, ApJ, 903, 77
Calzadilla, M. S., McDonald, M., Donahue, M., et al. 2022, ApJ, 940, 140
Choudhury, P. P., & Reynolds, C. S. 2022, MNRAS, 514, 3765
Choudhury, P. P., & Sharma, P. 2016, MNRAS, 457, 2554
Choudhury, P. P., Sharma, P., & Quataert, E. 2019, MNRAS, 488, 3195
Ciotti, L., Pellegrini, S., Renzini, A., & D'Ercole, A. 1991, ApJ, 376, 380
Collette, A. 2013, Python and HDF5 (Sebastopol, CA: O'Reilly & Associates)
Conroy, C., Gunn, J. E., & White, M. 2009, ApJ, 699, 486
Conroy, C., van Dokkum, P. G., & Kravtsov, A. 2015, ApJ, 803, 77
Crain, R. A., Schaye, J., Bower, R. G., et al. 2015, MNRAS, 450, 1937
Das, H. K., Choudhury, P. P., & Sharma, P. 2021, MNRAS, 502, 4935
Donahue, M., & Voit, G. M. 2022, PhR, 973, 1
Draine, B. T. 2011, Physics of the Interstellar and Intergalactic Medium (Princeton, NJ: Princeton Univ. Press)
El-Badry, K., Ostriker, E. C., Kim, C.-G., Quataert, E., & Weisz, D. R. 2019, MNRAS, 490, 1961
Fabian, A. C. 2012, ARA&A, 50, 455
Faucher-Giguère, C.-A., & Oh, S. P. 2023, ARA&A, 61, 131
Federrath, C., Klessen, R. S., & Schmidt, W. 2008, ApJL, 688, L79
Federrath, C., Roman-Duval, J., Klessen, R. S., Schmidt, W., & Mac Low, M. M. 2010, A&A, 512, A81
Fielding, D., Quataert, E., Martizzi, D., & Faucher-Giguère, C.-A. 2017, MNRAS, 470, L39
Fielding, D. B., Ostriker, E. C., Bryan, G. L., & Jermyn, A. S. 2020, ApJL, 894, L24
Gaspari, M., McDonald, M., Hamer, S. L., et al. 2018, ApJ, 854, 167
Gaspari, M., Ruszkowski, M., & Sharma, P. 2012, ApJ, 746, 94
Gaspari, M., Temi, P., & Brighenti, F. 2017, MNRAS, 466, 677
Gatuzz, E., Sanders, J. S., Dennerl, K., et al. 2023a, MNRAS, 520, 4793
Gatuzz, E., Sanders, J. S., Dennerl, K., et al. 2023b, MNRAS, 525, 6394
Guo, M., Stone, J. M., Kim, C.-G., & Quataert, E. 2023, ApJ, 946, 26
Harris, C. R., Millman, K. J., van der Walt, S. J., et al. 2020, Natur, 585, 357
Hernquist, L. 1990, ApJ, 356, 359
Hopkins, P. F., Chan, T. K., Garrison-Kimmel, S., et al. 2020, MNRAS, 492, 3465
Hunter, J. D. 2007, CSE, 9, 90
Huško, F., & Lacey, C. G. 2023, MNRAS, 521, 4375
Kempski, P., & Quataert, E. 2020, MNRAS, 493, 1801
Khatri, R., & Gaspari, M. 2016, MNRAS, 463, 655
Kim, C.-G., & Ostriker, E. C. 2015, ApJ, 802, 99
Konstandin, L., Girichidis, P., Federrath, C., & Klessen, R. S. 2012, ApJ, 761, 149
Lemaster, M. N., & Stone, J. M. 2009, ApJ, 691, 1092
Li, M., Li, Y., Bryan, G. L., Ostriker, E. C., & Quataert, E. 2020a, ApJ, 894, 44
Li, M., Li, Y., Bryan, G. L., Ostriker, E. C., & Quataert, E. 2020b, ApJ, 898, 23
Li, Y., Bryan, G. L., & Quataert, E. 2019, ApJ, 887, 41
Li, Y., Gendron-Marsolais, M.-L., Zhuravleva, I., et al. 2020c, ApJL, 889, L1
Li, Y.-P., Yuan, F., Mo, H., et al. 2018, ApJ, 866, 70
Main, R. A., McNamara, B. R., Nulsen, P. E. J., Russell, H. R., & Vantyghem, A. N. 2017, MNRAS, 464, 4360
Maoz, D., & Graur, O. 2017, ApJ, 848, 25
Martizzi, D., Faucher-Giguère, C.-A., & Quataert, E. 2015, MNRAS, 450, 504
McCourt, M., Sharma, P., Quataert, E., & Parrish, I. J. 2012, MNRAS, 419, 3319
McNamara, B. R., & Nulsen, P. E. J. 2007, ARA&A, 45, 117
Merritt, D., & Ferrarese, L. 2001, MNRAS, 320, L30
Mohapatra, R., Federrath, C., & Sharma, P. 2020, MNRAS, 493, 5838
Mohapatra, R., Federrath, C., & Sharma, P. 2021, MNRAS, 500, 5072
Mohapatra, R., Federrath, C., & Sharma, P. 2022, MNRAS, 514, 3139
Mohapatra, R., & Sharma, P. 2019, MNRAS, 484, 4881
Mohapatra, R., Sharma, P., Federrath, C., & Quataert, E. 2023, MNRAS, 525, 3831
Molero, M., Matteucci, F., & Ciotti, L. 2023, MNRAS, 518, 987
Okuta, R., Unno, Y., Nishino, D., Hido, S., & Loomis, C. 2017, Proc. of Workshop on Machine Learning Systems (LearningSys) in The Thirty-first Annual Conf. on Neural Information Processing Systems (NIPS), http://learningsys.org/nips17/assets/papers/paper_16.pdf
Olivares, V., Salome, P., Combes, F., et al. 2019, A&A, 631, A22
Olivares, V., Su, Y., Forman, W., et al. 2023, ApJ, 954, 56
Parrish, I. J., Quataert, E., & Sharma, P. 2009, ApJ, 703, 96
Parrish, I. J., Quataert, E., & Sharma, P. 2010, ApJL, 712, L194
Peterson, J. R., Kahn, S. M., Paerels, F. B. S., et al. 2003, ApJ, 590, 207
Pillepich, A., Springel, V., Nelson, D., et al. 2018, MNRAS, 473, 4077
Prasad, D., Sharma, P., & Babul, A. 2015, ApJ, 811, 108
Prasad, D., Sharma, P., & Babul, A. 2018, ApJ, 863, 62
Pulido, F. A., McNamara, B. R., Edge, A. C., et al. 2018, ApJ, 853, 177
Rafferty, D. A., McNamara, B. R., & Nulsen, P. E. J. 2008, ApJ, 687, 899
Romero, C. E., Gaspari, M., Schellenberger, G., et al. 2023, ApJ, 951, 41
Scannapieco, E., & Bildsten, L. 2005, ApJL, 629, L85
Sharma, P., McCourt, M., Quataert, E., & Parrish, I. J. 2012, MNRAS, 420, 3174
Smith, B. D., Bryan, G. L., Glover, S. C. O., et al. 2017, MNRAS, 466, 2217
Stone, J. M., Tomida, K., White, C. J., & Felker, K. G. 2020, ApJS, 249, 4
Su, K.-Y., Hopkins, P. F., Hayward, C. C., et al. 2019, MNRAS, 487, 4393
Tang, S., Wang, Q. D., Lu, Y., & Mo, H. J. 2009a, MNRAS, 392, 77
Tang, S., Wang, Q. D., Mac Low, M.-M., & Joung, M. R. 2009b, MNRAS, 398, 1468
Tang, X., & Churazov, E. 2017, MNRAS, 468, 3516
Tremblay, G. R., Combes, F., Oonk, J. B. R., et al. 2018, ApJ, 865, 13
Trott, C., Berger-Vergiat, L., Poliakoff, D., et al. 2021, CSE, 23, 10
Trujillo, I., Ferreras, I., & de La Rosa, I. G. 2011, MNRAS, 415, 3903
van der Velden, E. 2020, JOSS, 5, 2004
Virtanen, P., Gommers, R., Oliphant, T. E., et al. 2020, NatMe, 17, 261
Voit, G. M. 2018, ApJ, 868, 102
Voit, G. M. 2021, ApJL, 908, L16
Voit, G. M., Bryan, G. L., Prasad, D., et al. 2020, ApJ, 899, 70
Voit, G. M., Donahue, M., O'Shea, B. W., et al. 2015, ApJL, 803, L21
Wang, C., Ruszkowski, M., Pfrommer, C., Oh, S. P., & Yang, H. Y. K. 2021, MNRAS, 504, 898
Wang, S.-C., & Yang, H. Y. K. 2022, MNRAS, 512, 5100
Werner, N., Allen, S. W., & Simionescu, A. 2012, MNRAS, 425, 2731
Werner, N., Oonk, J. B. R., Canning, R. E. A., et al. 2013, ApJ, 767, 153
Werner, N., Oonk, J. B. R., Sun, M., et al. 2014, MNRAS, 439, 2291
Zhuravleva, I., Allen, S. W., Mantz, A., & Werner, N. 2018, ApJ, 865, 53
Zhuravleva, I., Churazov, E., Arévalo, P., et al. 2015, MNRAS, 450, 4184
Zhuravleva, I., Churazov, E., Schekochihin, A. A., et al. 2014, Natur, 515, 85